

1-1-1984

# The kinematics of the emission line gas in quasars and active galactic nuclei.

Timothy John Carroll  
*University of Massachusetts Amherst*

Follow this and additional works at: [https://scholarworks.umass.edu/dissertations\\_1](https://scholarworks.umass.edu/dissertations_1)

---

## Recommended Citation

Carroll, Timothy John, "The kinematics of the emission line gas in quasars and active galactic nuclei." (1984). *Doctoral Dissertations 1896 - February 2014*. 1778.  
[https://scholarworks.umass.edu/dissertations\\_1/1778](https://scholarworks.umass.edu/dissertations_1/1778)

This Open Access Dissertation is brought to you for free and open access by ScholarWorks@UMass Amherst. It has been accepted for inclusion in Doctoral Dissertations 1896 - February 2014 by an authorized administrator of ScholarWorks@UMass Amherst. For more information, please contact [scholarworks@library.umass.edu](mailto:scholarworks@library.umass.edu).

UMASS/AMHERST



312066 0024 2981 1



DATE DUE

OCT 12 1988			
NOV 1 1988			

UNIVERSITY LIBRARY  
UNIVERSITY OF MASSACHUSETTS  
AT  
AMHERST

PHYS SCI

LD  
3234  
M267  
1984  
C3197

THE KINEMATICS OF THE EMISSION LINE GAS  
IN QUASARS AND ACTIVE GALACTIC NUCLEI

A Dissertation Presented

By

TIMOTHY JOHN CARROLL

Submitted to the Graduate School of the  
University of Massachusetts in partial fulfillment  
of the requirements for the degree of

DOCTOR OF PHILOSOPHY

February 1984

Astronomy

THE KINEMATICS OF THE EMISSION LINE GAS  
IN QUASARS AND ACTIVE GALACTIC NUCLEI

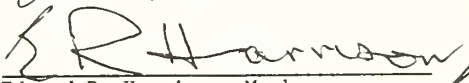
A Dissertation Presented

By

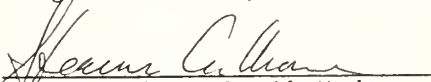
TIMOTHY JOHN CARROLL

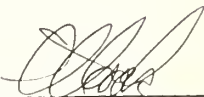
Approved as to style and content by:

  
\_\_\_\_\_  
John Y. Kwan, Chairman of Committee

  
\_\_\_\_\_  
Edward R. Harrison, Member

  
\_\_\_\_\_  
George S. Greenstein, Member

  
\_\_\_\_\_  
Stearns A. Morse, Outside Member

  
\_\_\_\_\_  
Leroy F. Cook, Department Head  
Physics and Astronomy

## ACKNOWLEDGEMENTS

Of all of the people who have contributed to my scientific education, the three with whom I have worked here at the University of Massachusetts have been the most influential. It was my great good fortune that Prof. John Kwan arrived at the University at a time when I was frantically searching for a dissertation topic. He is an excellent scientist and a patient and meticulous teacher; it is he who has taught me what it means to "do science". Both Prof. George Greenstein and Prof. Edward Harrison have encouraged me with their ideas, support and interest. I hope that I am fortunate enough to have acquired the best of their habits, and I am indebted to each of these three men.

I must also thank my many friends and fellow students, both here and elsewhere, who have supported me through this endeavor.

My parents, too, have been very patient in waiting many years for my final graduation. I am grateful to them for allowing me to choose my own path.

Finally, I wish to thank the anonymous taxpayers. Though they do not understand what it is that we do, they willingly and generously provide the means by which we pursue our esoteric interests.

ABSTRACT

The Kinematics of the Emission Line Gas  
in Quasars and Active Galactic Nuclei

(February 1984)

Timothy J. Carroll, B.S., Massachusetts Institute of Technology

M.S., Ph.D., University of Massachusetts

Directed by: Professor John Y. Kwan

We propose a kinematic model in which the broad-line emission clouds orbit the central continuum source in nearly parabolic orbits in order to produce a symmetric Ly $\alpha$  profile in spite of the angular asymmetry in the Ly $\alpha$  emission from an individual optically-thick cloud. Theoretical profiles are generated and compared with logarithmic line shapes, and the pros and cons of this model and others proposed are discussed.

We next examine the forbidden line spectrum of quasars and Seyfert galaxies in light of the various proposed kinematic models for the broad-line regions of these objects. Gravitational infall models predict significant forbidden line emission at velocities  $< 10^3$  km s $^{-1}$ . Different emission line widths are obtained for different lines dependent upon their respective critical densities for collisional de-excitation; lines with higher critical densities will have broader profiles. Ballistic outflow and radiative acceleration models are found to produce negligible forbidden line emission at these velocities.

The parabolic-orbital model (Kwan and Carroll 1982) for the broad

emission line regions of quasars and Seyfert galaxies is then extended and improved to include the effects of a finite infalling cloud number and size. Disruption of the cloud by tidal forces results in a large velocity dispersion among the resulting fragment cloudlets. This velocity dispersion compensates for the small number of clouds at high velocity so that a fairly smooth profile is obtained.

The drag of a confining intercloud wind is also considered. The major dynamical effect of this drag is to trap clouds with less than a certain angular momentum. The trapping of clouds produces an asymmetry in the Ly $\alpha$  profile due to the absence of an outward leg for the trapped clouds. The asymmetry is reduced by the spiralling of the trapped cloud material, and it shows up mainly in the core and far wings of the profile.

The dependence of various line emissivities on the incident ionizing flux has been computed by Kwan (1983). His results are convolved with the cloud velocity dispersions, and the resulting emission line profiles demonstrate that the gravitational model can reproduce the observed broadness of HeI $\lambda$ 5876 relative to H $\beta$  (Shuder 1982).



TABLE OF CONTENTS

ACKNOWLEDGEMENT . . . . .	iii
ABSTRACT . . . . .	iv
Chapter	
I. INTRODUCTION . . . . .	1
II. THE PARABOLIC-ORBITAL MODEL . . . . .	9
Introduction . . . . .	9
The Line Profile . . . . .	10
Discussion . . . . .	20
III. THE ASSOCIATED FORBIDDEN LINE EMISSION . . . . .	26
Introduction . . . . .	26
The NLR Spectrum . . . . .	28
Broad-Line Kinematic Models and the Associated Forbidden Line Emission . . . . .	46
Model Profiles and Intensities . . . . .	56
Conclusions . . . . .	70
IV. THE EXTENDED MODEL . . . . .	72
Introduction . . . . .	72
The Model . . . . .	75
Model Profiles . . . . .	85
Summary . . . . .	121
V. SUMMARY AND FUTURE WORK . . . . .	124
. . . . .	. . . . .
BIBLIOGRAPHY . . . . .	128
APPENDIX . . . . .	133

LIST OF TABLES

1. Theoretical and Experimental Forbidden Line Intensities . . . .	34
2. Radial Intensity Dependence . . . . .	58

LIST OF ILLUSTRATIONS

1.	Lya Profiles for Different Angular Emissivity Dependences . .	16
2.	Comparison of Logarithmic Profile With Parabolic-Orbital Model Lya Profiles . . . . .	18
3.	Comparison of CIV $\lambda$ 1549 and CIII] $\lambda$ 1909 Profiles . . . . .	23
4.	Dependence of Diagnostic Line Ratios on $N_O$ and $\Gamma^i$ . . . . .	31
5.	Temperature-Density Diagnostic Plot for Seyfert Galaxies . . .	35
6.	Density Dependence of High Ionization Line Emission . . . . .	41
7.	Density Dependence of Low Ionization Line Emission . . . . .	43
8.	Density Dependence of [OIII] $\lambda$ 5007 Emission for Expanding Cloud . . . . .	50
9.	Forbidden Line Profiles . . . . .	61
10.	Line Profiles for a Trapped Cloud Ensemble . . . . .	87
11.	Line Profiles for a Trapped Cloud Ensemble . . . . .	95
12.	Line Ratios as a Function of Velocity . . . . .	103
13.	Line Profiles for Escaping Cloud Ensemble . . . . .	107
14.	Lya Profiles for Different Angular Emissivity Dependences . .	113
15.	CIV $\lambda$ 1549 Profiles With and Without Area Projection . . . . .	118

## CHAPTER I

### INTRODUCTION

At this writing, the study of the enigmatic objects known as quasars (also referred to as quasi-stellar objects or QSO's) has proceeded for two decades. First discovered as radio objects, their distinctive character was not realized until Mathews and Sandage (1963) made the first optical identifications of a peculiar blue "radio star" with each of three catalogued compact radio sources. The optical spectra obtained from these objects at Palomar were described by the authors as "extremely peculiar", with several very broad, strong, and unidentified emission features present. Schmidt's (1963) astute notion that the peculiar spectra observed in these objects were due simply to a cosmologically large redshift of the Balmer emission spectrum provided the key to most of what we now know about quasars.

While simple, Schmidt's explanation had remarkable implications. First, the interpretation of the observed redshifts as due to the cosmologic expansion implied that quasars lie at distances greater than most known galaxies. Yet, quasars are remarkably bright so that derived luminosities, assuming a cosmologic distance, must exceed  $10^{46}$  ergs  $s^{-1}$  in the optical region alone. Recent infrared and X-ray spectroscopy has indicated that the integrated luminosity at these wavelengths may be even greater. These luminosities are at least 100 times larger than that of a large galaxy such as our own, and observations of variation in the continuum strength over a time scale of months implies, from

light travel time arguments, that this radiation is produced in a region of diameter  $d \ll 0.1$  pc across. This result provoked many astronomers to discount the cosmologic interpretation and seek other more palatable explanations. A lucid discussion of many of these alternative ideas can be found in Field, Arp, and Bahcall (1973). For various reasons, each of these alternatives can be discounted, and today the consensus is that quasars do lie at distances given by their redshifts. The search for an understanding of the production mechanism for the intense continuum radiation has spawned much theoretical work on black holes and accretion disk dynamics, but observational support for specific models is lacking. For the purposes of this dissertation, we shall take the existence of the radiation continuum as a given, and we leave the question of the origin of the radiation for other workers. Instead, we will pursue what has been a more fruitful line of investigation by considering the effects of this radiation on the material surrounding the quasar "engine". Proceeding in this way, some inferences about the nature of the continuum source can be made.

While not so surprising as the deduction of extreme luminosities for quasars, a more important practical result of Schmidt's discovery was to allow the established field of nebular spectroscopy to be brought to bear on the problem of the quasar emission lines. Due to the different conditions for excitation of emission lines from a variety of elements and ionization stages, a comparison of observed relative line strengths with theoretically derived values can yield far more information about physical conditions at the quasar than can the featureless

continuum. Line profile shapes as well contain information on the kinematics of the gas responsible for the line emission. Much theoretical work has been done, but conclusive results have been hampered, until recently, by technological limitations on the quality of the spectra obtainable from these objects.

Given the limits of instrumental resolution and the pioneering nature of observations in the early days of quasar research, only general qualitative statements could be made about the observed line shapes. Observations of quasars with different redshifts allowed ground based observers to sample different portions of the spectrum through the optical window. From this process, it was realized that a typical spectrum is characterized by intense emission lines from a wide range of atomic ionization states. The lines could be separated on the basis of the width of their profiles. Permitted emission lines were observed to have very broad profiles with  $\text{FWHM} > 10000 \text{ km s}^{-1}$  and a profile shape characterized as logarithmic in that the profile wings could often be fit by a functional form  $f_v \sim \ln(v_{\text{max}}/v)$  where  $v$  is the doppler velocity shift from line center and  $v_{\text{max}}$  is some maximum velocity. The forbidden lines, however, are much narrower with  $\text{FWHM}$  of only  $\sim 500 \text{ km s}^{-1}$ . Within each group, different lines were judged to have similar profiles.

The large inferred velocities for the broad-line emission are most reasonably attributed to bulk motion of the emitting gas. The first successful kinematic model to explain the observed broad-line profile shapes reasoned that the intense ionizing radiation incident upon the

emitting gas must transfer substantial momentum as well. Blumenthal and Mathews (1975) were able to show that fully ionized clouds could be accelerated to the observed velocities by the quasar continuum. Gas clouds which are optically thick to the ionizing continuum are inefficiently accelerated. A notable success of this model was the prediction of a logarithmic line shape, provided that emitting clouds are all formed at the same radius and a constant mass flow is maintained. A logarithmic shape is not unique to the radiative acceleration model, however, as demonstrated by Capriotti, Foltz, and Byard (1979). Those authors pointed out that radiative acceleration or gravitational infall of optically thick clouds, and a non-steady state ballistic outflow resulting from an explosive expulsion of material from the quasar center all predict such a shape. Further progress on understanding the nature of the kinematics of the emitting gas would have to wait for better observations of the profiles and a more detailed understanding of the physical properties of the emission line gas.

Quantitative spectral intensity information is more easily obtainable than high resolution profiles, so early theoretical work concentrated on explaining the relative line strengths. It was realized early on that the observed spectral intensities were very similar to the spectrum of photoionized galactic nebulae. Most differences could be explained by the difference in the ionizing continuum: galactic nebulae are ionized by black-body radiation from hot O and B stars while the quasar continuum follows a power law form. Early photoionization models employing this harder continuum and solar elemental abun-

dances were generally successful in explaining the relative intensities of the various lines. The characteristic physical conditions for the emitting gas can be derived by comparing various theoretical models with the observations. Nucleon gas densities of  $N_O \sim 10^4 \text{ cm}^{-3}$  and  $N_O > 10^9 \text{ cm}^{-3}$  are typically derived numbers for the narrow-line and broad-line gas respectively. The incident radiation intensity is described by an ionization parameter  $\Gamma^i = N_{ph}/N_O$  with  $N_{ph}$  the ionizing photon number density. A typical model ionization parameter is  $\Gamma^i > 0.03$  for both emission line regions. Coupling the derived density and ionization parameter with the typical quasar luminosity  $L \sim 10^{46} \text{ erg s}^{-1}$  yields a characteristic distance of  $\sim 1 \text{ pc}$  for the broad-line region and  $\sim 300 \text{ pc}$  for the narrow line region. Davidson and Netzer (1979) provide an extensive review of the history and methodology of these computations.

Lack of observed continuum absorption at the Lyman edge implies that the emission line gas cannot uniformly cover the continuum source. A total covering factor of  $f \sim 0.1$  is a typically derived value (Oke 1974; Osmer 1979; Smith et al. 1979). The maximum column density which can be ionized by the incident radiation is equal to the number of recombinations per unit area  $N_c = \Gamma^i c / \beta \approx 10^{21} \text{ cm}^{-2}$  where  $c$  is the speed of light and  $\beta$  is the hydrogen case B recombination coefficient. For a gas density of  $10^9 \text{ cm}^{-3}$ , this corresponds to a linear dimension of  $10^{12} \text{ cm}$ . Optically thick clouds could have a large zone of neutral material beyond the fully ionized region, but this will still be much smaller than the size of the broad emission line region ( $\sim 1 \text{ pc}$ ). The



picture that emerges of the emission line gas distribution is of a large number of small clouds or filaments distributed throughout the emitting region.

A synthetic spectrum compiled by Baldwin (1977) to represent the typical quasar, however, uncovered a difficult problem for the theoretical photoionization models to solve. Specifically, Baldwin found that the intensity ratio of Ly $\alpha$  to H $\beta$  was anomalously low compared to what one would expect from a normal recombination spectrum, and this was subsequently confirmed by direct UV observations (Wu 1977; Davidsen, Hartig and Fastie 1977). The same was found to be true of the H $\beta$ /H $\alpha$  ratio. Reddening of the emission line spectrum, due to dust for instance, could qualitatively explain these observations, but this raises other questions. Why is dust present in such primitive objects, yet no heavy element depletion is observed from the emitting gas (Gaskell, Shields, and Wampler 1981)? How does the dust form, and how does it survive in such a hostile environment? Recent observations have also shown that the Pa $\alpha$ /H $\alpha$  ratio is less than the recombination value in quasars (Soifer et al. 1981) indicating that reddening cannot be very important. A more elegant solution was discussed by Kwan and Krolik (1979, 1981).

Kwan and Krolik (1979, 1981) were able to show that this problem could be solved if the emitting clouds were very optically thick to Ly $\alpha$ . In this case, an extended region of predominantly neutral hydrogen will exist beyond the point where the Lyman continuum between 13.6 and 54.4 eV has been absorbed. Ionization by X-rays heats the gas and main-

tains a significant electron fraction ( $f_e \sim 0.1$ ) due mainly to collisional ionization of hydrogen. Significant H $\beta$  emission is produced due to collisional population of the  $n=2$  level. Collisionally generated Ly $\alpha$  photons, however, are trapped by the large neutral hydrogen column densities and consequently do not escape the cloud before being thermalized by electron collisional de-excitation. In this way, H $\beta$  is enhanced, and the Ly $\alpha$ /H $\beta$  ratio thereby reduced.

Many other emission lines of widely varying ionization level are produced in the extended ionized zone of an optically thick cloud. Thus, this circumstance also provides an understanding of why such lines as CIV $\lambda$ 1549 and MgII $\lambda$ 2798 appear to have similar profiles. The hypothesis of optically thick clouds, however, confronts all theoretical models for the kinematics of the emission line gas with a serious constraint. All models employing optically thick clouds and predominantly radial motion for the clouds will predict a strong asymmetry in the Ly $\alpha$  profile. Outflow models will have weaker blue emission, while inflow models will predict weaker red emission. Ly $\alpha$  profiles are generally observed to be completely symmetric (Wilkes and Carswell 1982; Wilkes 1983). In response to this problem, Kwan and Carroll (1982) proposed a variation of the simple radial gravitational infall model. By the simple expedient of invoking a small non-zero angular momentum for the infalling clouds, their gravitational model was able to provide for both infall and outflow as the clouds orbit the quasar center in nearly parabolic orbits. This dissertation discusses and further develops the parabolic-orbital model for the kinematics of the quasar emission line region.

The body of this dissertation comprises three main chapters, each of which has been or will be published by the Astrophysical Journal. Chapter II presents the parabolic orbital model and demonstrates how it can reasonably give profiles from an ensemble of optically thick clouds in agreement with the observations. Chapter III discusses some of the implications of a gravitational infall model for the narrow-line emission region and suggests a possible interplay between the narrow and broad-line regions. Chapter IV presents a more detailed and realistic version of the model by incorporating the effects of tidal and quasar wind drag forces on the cloud dynamics, as well as the effects of a finite cloud number on the profile smoothness and structure. Chapter V will summarize the results of the previous chapters, and directions for future research will also be discussed.

CHAPTER II  
THE PARABOLIC-ORBITAL MODEL

Introduction

The widths of the broad emission lines in quasar and Seyfert type 1 spectra extend over a range of  $\sim 10^4$  km s<sup>-1</sup>. It is generally believed that they arise from bulk motion of a large number of small clouds close to the continuum source (see the review by Davidson and Netzer 1979). Much work has been done to compare theoretical line profiles, generated under different assumptions of the cloud kinematics, with observed ones in order to deduce the nature of the motion, whether it be outflow, infall, or rotation (Blumenthal and Mathews 1975, Shields 1978, Capriotti, Foltz, and Byard 1980). Models involving outflow were usually favored.

One property of an individual broad-line cloud that has become evident is that it is very optically thick to the Lyman continuum. The profiles of lines that are produced at appreciable Lyman continuum optical depths (e.g. OI $\lambda$ 8446, MgII $\lambda$ 2798) are usually quite similar to those of the Balmer lines and lines of highly ionized elements (Davidson and Netzer 1979, Grandi and Phillips 1979, Grandi 1980), and recent photoionization calculations show that the relative fluxes of Ly $\alpha$ , H $\beta$ , and other emission lines are roughly reproduced in model clouds of large optical depths (Kwan and Krolik 1979, 1981; Canfield and Puetter 1980; Weisheit, Shields, and Tarter 1981). The Ly $\alpha$  emission from such a cloud is highly anisotropic, i.e., most of the

$\text{Ly}\alpha$  radiation emerges from the face of the cloud illuminated by the continuum source (Ferland and Netzer 1979, Kwan and Krolik 1981). This effect then places a constraint on kinematic models. For example, in cases of radial motion (either infall or outflow), the  $\text{Ly}\alpha$  profile is expected to be very asymmetric. Observed profiles, on the other hand, are symmetric and similar to those of CIV $\lambda$ 1549 and CIII] $\lambda$ 1909 (e.g. Boggess et al. 1979, Oke and Zimmerman 1979, Weymann 1981).

To produce a symmetric  $\text{Ly}\alpha$  profile from an ensemble of optically-thick clouds, we propose the following kinematic model. We assume that the clouds are moving in nearly parabolic orbits about the continuum source. We envision the infall of matter (one possible source is from cloud-cloud collisions in the narrow-line emission region) with a range of impact parameters. The subsequent motion is dictated primarily by gravitational attraction of the central object. The kinematic situation is quite analogous to the case of comet motion about the Sun. Since both inward and outward motion are present, the  $\text{Ly}\alpha$  profile should be less influenced by anisotropy in the emission from an individual cloud. In the next Section we generate theoretical profiles to compare with observations, and in §III we discuss the pros and cons of this kinematic model and other existing ones.

### The Line Profile

We use numerical techniques to generate the line profile produced by a spherical distribution of clouds orbiting a central object in

nearly parabolic orbits. To illustrate how the line profile depends on the cloud properties, however, analytical derivations are useful, and we study them first before presenting the numerical results.

Since the orbits are highly eccentric, we can facilitate the analytical derivation by making the rough approximation that each orbit comprises simply a leg of radial inward motion and a leg of radial outward motion. We consider first the profile generated from the inward leg. After some algebraic manipulation, the line profile  $I(v)$  (ergs per sec per unit velocity interval) for a steady, spherical-symmetric, radial infall can be written in the form

$$I(v) \propto \int_r \int_{\theta} \frac{\epsilon(r)\phi(\theta) \delta [v + v'(r)\cos\theta] \sin\theta d\theta dr}{v'(r)} \quad . \quad (\text{II-1})$$

Here  $r$  is the radial distance from the central object,  $\theta$  the angle between the line of sight and the radius vector, and  $v'(r)$  the magnitude of the infall velocity. The symbol  $\delta$  is the delta function,  $\epsilon(r)$  is the total rate of Ly $\alpha$  emission (ergs s $^{-1}$ ) from a cloud, and  $\phi(\theta)$  is the fraction of that emission towards the observer. In the numerical simulation, we considered two possible choices for  $\phi(\theta)$ ; they are:

$$\phi_1(\theta) = \begin{cases} 2 \cos\theta & 0 < \theta < \pi/2 \\ 0 & \pi/2 < \theta < \pi \end{cases} \quad , \quad (\text{II-2})$$

and

$$\phi_2(\theta) = \begin{cases} 1 & 0 < \theta < \pi/2 \\ 0 & \pi/2 < \theta < \pi \end{cases} \quad . \quad (\text{II-3})$$

Both choices assume that the Ly $\alpha$  radiation emerges from the illuminated face of the cloud only. In the first choice, the observed emission is proportional to the projected area of the illuminated surface on the plane of the sky; in the second choice, it is independent of  $\theta$  as long as the illuminated face is orientated towards the observer. Given our ignorance of the actual cloud geometry, we believe the realistic situation is likely to be somewhere in between those two choices. In situations in which the Ly $\alpha$  emission does not have a significant asymmetry between front and back emission, and for other emission lines, a more appropriate choice for  $\phi(\theta)$  is that it be independent of  $\theta$  for  $0 < \theta < \pi$ .

For  $\phi(\theta) = \phi_2(\theta)$ , equation (1) is readily reduced to:

$$I(v) \propto \int_{-v}^{v'_{\max}} \frac{r^2 \epsilon(r) dv'}{v'} \quad \text{for } v < 0 \quad . \quad (\text{II-4})$$

In the case in which the cloud is optically thick to the Lyman continuum,  $\epsilon(r)$  is proportional to  $A(r)/r^2$ , where  $A$  is the area of the illuminated face.

A logarithmic profile, which is a good fit to observations (e.g. Blumenthal and Mathews 1975, Capriotti, Foltz, and Byard 1980) will then be obtained if the cloud area  $A$  is constant. For  $\phi(\theta) = \phi_1(\theta)$ , and  $A$  constant, the profile is triangular.

We envision that during its motion a given cloud is always in pressure equilibrium with a hot ambient medium. The latter is expected to develop a wind as its sound speed will exceed the local escape velo-

city beyond a certain radius. Judging from the calculations by Krolik, McKee, and Tarter (1981) on the physical conditions of the hot intercloud gas, we believe an isothermal wind is likely, so that the intercloud pressure decreases roughly as  $r^{-2}$  far away from the continuum source. To adjust to the external pressure, the density in the cloud,  $n$ , will then vary roughly as  $r^{-2}$ . The wind pushes against the infalling cloud. In order for gravity to overcome that outward force, the central mass  $M$  and the column density  $N$  of the cloud must be such that  $MN > pr^2/GM_H$ , where  $p$  is the cloud pressure, and we have assumed that it is at least equal to the wind pressure. In the case of quasars, a central mass  $M > 5 \times 10^9 M_\odot$  is required to produce the high velocities observed in the line wings, if the broad-line emission occurs at about 1 pc from the central source. The above condition then imposes a constraint on the size of the cloud when it begins its inward motion. For example, if  $p \sim (2 \times 10^9 \text{ cm}^{-3} \times k \times 2 \times 10^4 \text{ K})(1 \text{ pc}/r)^2$ , the column density  $N$  would need to be  $\sim 5 \times 10^{22} \text{ cm}^{-2}$ , and the cloud is very optically thick to the Lyman continuum. As the cloud falls in, we expect it to adjust to the increasing intercloud pressure by being compressed primarily along the direction towards the central object, and becomes highly flattened. The illuminated face of the cloud then retains a roughly constant area, and numerical simulation of the evolution of the cloud shape demonstrates this. Close to the central source, however, the cloud will break up into many smaller clouds or cloudlets, owing to the different angular momenta of its constituent parts. As each cloudlet moves around the central source, its motion is no longer



predominantly radial, and we cannot ascertain whether it is highly flattened or spherical in shape. In the latter situation, the area of the cloudlet varies as  $n^{-2/3}$  or  $r^{4/3}$ . We consider two cases then in attempting to model the Ly $\alpha$  emission:

$$\text{case A : } r^2 \epsilon(r) \propto A(r) = \text{constant} \quad (\text{II-5})$$

$$\text{case B : } r^2 \epsilon(r) \propto A(r) = \begin{cases} \text{constant} , & r > 1 \text{ pc} \\ \text{constant} \times \left(\frac{r}{1 \text{ pc}}\right)^{4/3} , & r < 1 \text{ pc} \end{cases} \quad (\text{II-6})$$

In case B, the place where the radial dependence of  $\epsilon(r)$  changes is taken to be 1 pc, as that is roughly the size of the quasar broad-line emission region.

We consider next the emission from the outward leg of the orbital motion. Near the central source, the emission from the ensemble of cloudlets is analogous to that produced in the corresponding inward motion. Far away, however, the cloudlets will not merge back into a single large cloud. Instead, each one is likely to expand spherically as it adjusts to the decreasing external pressure, and will be accelerated by the intercloud wind. The Ly $\alpha$  emission from the ensemble during that part of the outward motion will not have a front-back asymmetry, since each cloudlet eventually becomes optically thin, and the shadowing among the cloudlets is small. It decreases rapidly with increasing  $r$ , however, as the emission rate  $\epsilon(r) \propto n \propto r^{-2}$ .

To determine the Ly $\alpha$  profiles produced under the different situations, we have performed numerical calculations assuming a central mass

of  $5 \times 10^9 M_{\odot}$  and spherical symmetry in the orientation of the orbits. In calculating the orbital motion, radiative acceleration and drag have been neglected. Figure 1 shows the profiles produced in case A (eq. I-5) when each orbit has an angular momentum of  $3500 \text{ km s}^{-1} \text{ pc}$ . The emission from the outward leg is assumed to be similar to that from the inward leg, so that only one half of the symmetric profile about line center is presented. The difference between the solid and dash curves represents the emission produced beyond 5 pc from the central source, and is quite small. In the real situation, the emission from the outer part of the outward leg is different from that of the inward leg, but since the former is expected to be symmetrical about line center, any asymmetry in the actual Ly $\alpha$  profile would arise from the emission in the early part of the infall, and would appear as a small excess in blueward emission. Even the emission from the inner parts of the orbital motion might have a small asymmetry, because of possible effects from drag, and cloud-cloud collisions which we have not considered.

Figure 2 compares the theoretical line profiles with logarithmic line shapes. The orbits have angular momenta evenly distributed between  $2000 \text{ km s}^{-1} \text{ pc}$  and  $5000 \text{ km s}^{-1} \text{ pc}$ . The calculations have ignored the difference in emission between the inward and outward motion. When the profiles are judged at intermediate and high velocities (emission produced close to the central source) where the calculations are more likely to portray the actual situation, they are reasonable matches to logarithmic shapes. The calculated profiles have extended wings at high velocities, but do not appear to be as pronounced as observed at some sources (e.g. Wu, Boggess, and Gull 1981).

Fig. 1. Theoretical profiles of Ly $\alpha$  emission from orbiting clouds. Upper and lower plots are obtained using the angular dependences of the Ly $\alpha$  emission given in equations (II-2) and (II-3) respectively. The solid and dash curves show the profiles due to emission from within 300 pc and within 5 pc respectively.

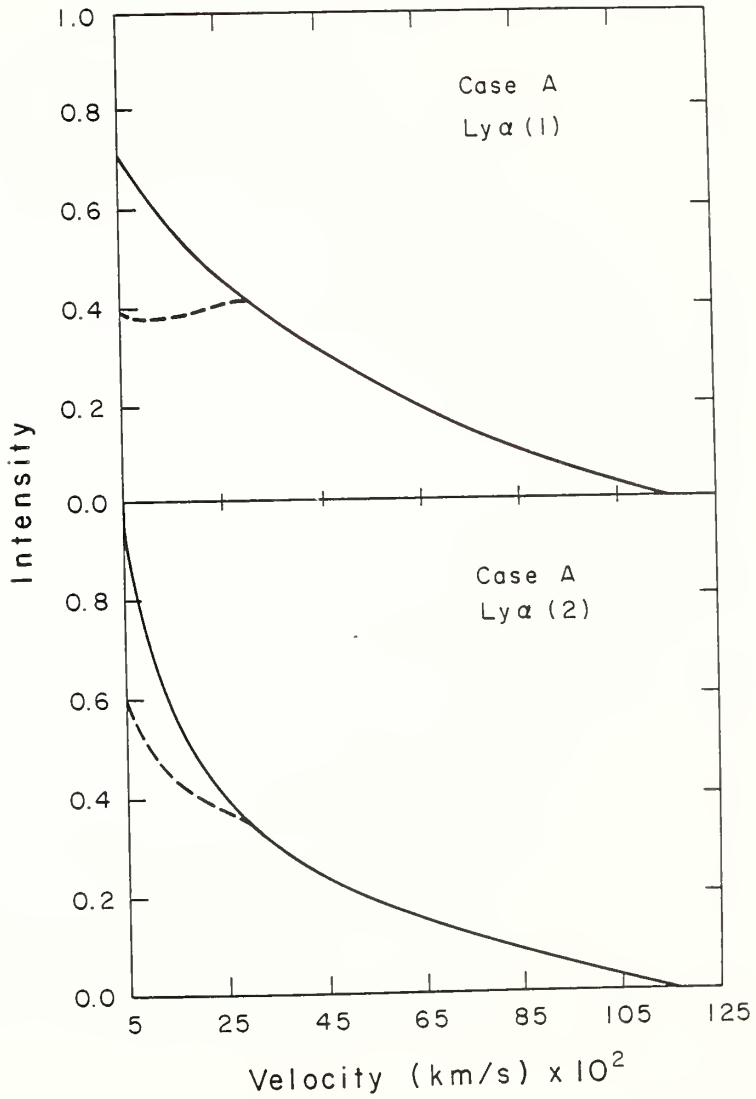
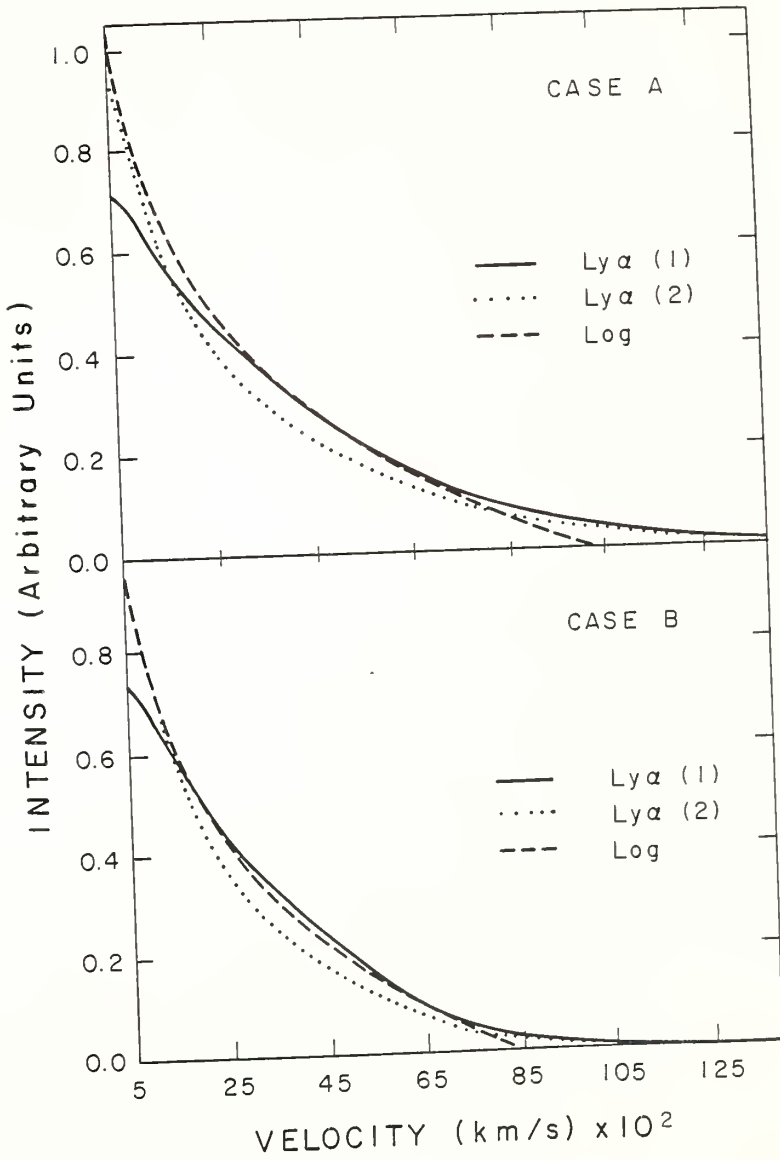


Fig. 2. Comparison of theoretical Ly $\alpha$  profiles, in both case A and case B, with logarithmic line shapes. Solid and dotted curves refer to angular dependences of the Ly $\alpha$  emission given by equations (II-2) and (II-3) respectively.



### Discussion

The kinematic model we have proposed allows for a more symmetric line profile than is possible in the case of radial outflow or infall. This difference aside, the various models proposed have different pros and cons, and we discuss them below.

In the model in which the broad-line clouds are accelerated by radiation pressure, logarithmic line profiles are readily obtained for both optically thin and optically thick clouds (Blumenthal and Mathews 1975, Mathews 1981)<sup>1</sup>.

---

1 For highly flattened, optically thick clouds, the angular dependence of the Ly $\alpha$  emission is not likely to be isotropic, even if the front-back asymmetry is ignored. If the observed emission is taken to be proportional to the projected area of the cloud on the plane of the sky, the line profile is triangular.

---

For an optically thick cloud, the acceleration from zero to the terminal velocity occurs over a small distance span. This ensures a narrow range in the physical properties (e.g. ionization parameter, density) of the emission gas, as suggested by observations, but would require that the clouds be formed and accelerated at the same radius. A difficulty with this model is the formation of the clouds, and in such a way that they are optically thick to the Lyman continuum, and yet not so optically thick that they cannot be accelerated to high velocities. In the model in which the clouds are ejected ballistically

(Capriotti, Foltz, and Byard 1980), the problem of cloud formation is negated. Logarithmic line profiles may not always be produced, however, as they depend on the distribution of the mass loss as a function of ejection speed, the deceleration due to gravity, and the evolution of the cloud shape during its motion. Conditions also need be chosen such that the covering factor by the clouds is small.

The presence of P-Cygni profiles at some quasars is usually cited as support for outflow models of the broad-line emission gas. Although there is no question that outflows are present at those quasars, it must be noted that those outflows have very different characteristics from those of the broad-line emission gas. Along our line of sight, those outflows cover uniformly the whole continuum source, and possibly the broad-line emission region, at every velocity over a range of  $\sim 3000 \text{ km s}^{-1}$  (Turnshek et al. 1980), whereas the broad-line clouds cover no more than about a tenth of the continuum source in total, and the velocity dispersion within an individual cloud is small,  $\sim 10 \text{ km s}^{-1}$ . For the same reason, those outflows involve a considerably greater amount of mass than is associated with the broad-line gas. It appears that they represent individual events of violent expulsions of matter, and do not share the same cause that is responsible for the acceleration of the individual broad-line clouds. In models in which the kinematics of the broad-line clouds have a gravitational origin, the presence of P-Cygni profiles at some quasars can be just as easily accommodated as being due to occasional explosions from those quasars, which temporarily obliterate the observational con-

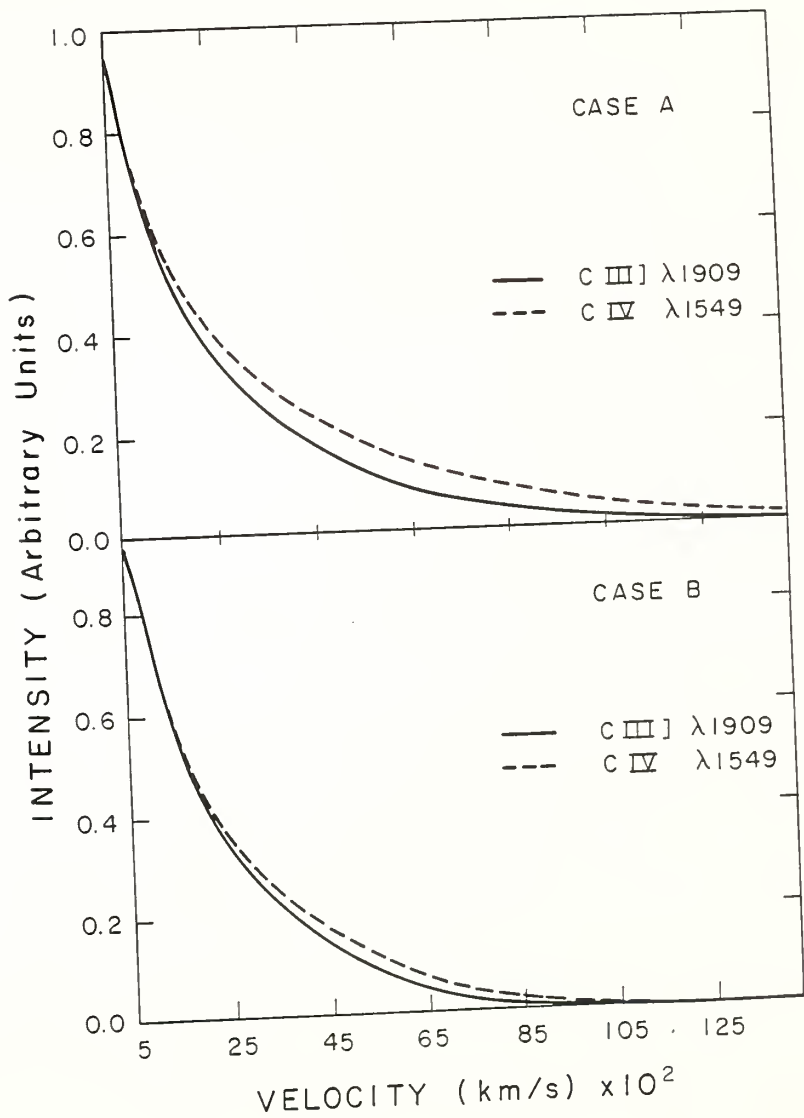


sequence of the emission-line clouds.

Keplerian rotational motion has been suggested for the broad-line gas of Seyfert nuclei (Osterbrock 1978). Such motion, however, does not readily produce logarithmic profiles (Capriotti, Foltz, and Byard 1980), and the frequency distribution of observed line widths is unlike that expected from a random orientation of an emission disk (Richstone, Ratnatunga, and Schaeffer 1980).

In all kinematic models in which the motion of the clouds is accelerated by gravity, there is a correlation between cloud velocity and density (Shields 1978). An argument against these models is that the line width of CIII] $\lambda$ 1909 is not observed to be narrower than that of CIV] $\lambda$ 1549. Figure 3 shows the calculated profiles of those two lines, with the CIII] $\lambda$ 1909 emission being reduced by a factor of  $(5 \times 10^8 \text{ cm}^{-3} / n)^{0.4}$  when the density in the cloud, equal to  $10^9 \text{ cm}^{-3} (1 \text{ pc} / r)^2$ , exceeds  $5 \times 10^8 \text{ cm}^{-3}$  (Kwan and Krolik 1981). Indeed the normalized CIII] $\lambda$ 1909 emission is weaker, but only prominently at high velocities, especially in case B. A firm conclusion of the relative width of those two lines may require high signal-to-noise observations at the line wings. Also, there is indication that several weak lines may contribute to the CIII] $\lambda$ 1909 emission (Gaskell, Shields, and Wampler 1981), and therefore to its line width. An advantage of models of cloud acceleration by gravity is the provision of a continuous supply of matter for the central source. For example, in the model we propose, cloud-cloud collisions in the broad-line region (with probability about twice the cloud covering factor), as well as direct radial

Fig. 3. Comparison between theoretical CIV $\lambda$ 1549 and CIII $\lambda$ 1909 profiles.



infall, will channel matter into the central source.

All things considered, we believe that gravitational acceleration of the broad-line clouds is not any more difficult to reconcile with observations and our present knowledge of the region as either radiative or ballistic acceleration. It deserves more consideration and scrutiny.

Several observations may test the kinematic model we propose. Besides the comparative weakness of CIII] $\lambda$ 1909 emission at the line wings, the model predicts weak emission of [OIII] $\lambda$ 5007 at intermediate velocities (up to  $\sim 2000 \text{ km s}^{-1}$ ). The Ly $\alpha$ /H $\beta$  ratio is expected to increase if it is measured over a smaller and smaller velocity interval about line center. The model requires a central mass  $> 10^{10} M_{\odot}$  in the case of quasars, and  $> 10^9 M_{\odot}$  in the case of Seyfert nuclei. If the region of narrow-line emission is resolved, an upper limit on the central mass can be derived.

A small fraction of Seyfert 1 galaxies have Balmer lines that are somewhat asymmetric (Osterbrock 1977). Possible explanations for the profile asymmetry require large Balmer optical depths or the presence of dust (Ferland, Netzer, and Shields 1979, Capriotti, Foltz, and Byard 1981). Either case produces a much stronger asymmetry in Ly $\alpha$ . The resolution of the Balmer line asymmetry will have to await the availability of Ly $\alpha$  profiles and the understanding of the kinematics they imply.

C H A P T E R    I I I  
THE ASSOCIATED FORBIDDEN LINE EMISSION

Introduction

The canonical optical emission line spectrum of quasars and Seyfert 1 galaxies [see e.g. Davidson and Netzer 1979] exhibits lines which, based on line width alone, can be separated into two distinct groups. Broad lines with FWHM  $> 10^4$  km s<sup>-1</sup> are easily discernible from the narrow lines with FWHM of only  $\sim 500$  km s<sup>-1</sup> typically. These widths are generally thought to arise from bulk motion of the emitting gas. A notable feature of this classification according to line width is that permitted and forbidden lines invariably fall into the broad and narrow line categories respectively. Apparently, conditions are such that the forbidden lines are excluded from the region of high velocity. A reasonable explanation for this is that high velocities and permitted line formation are associated with high densities, high enough so that the forbidden lines are suppressed. The forbidden lines would then necessarily be formed in a distinct region of lower density and velocity.

With this separation of the line formation problem into one of a forbidden narrow line region and a permitted broad line region (hereafter NLR and BLR respectively), the emission line intensities can be understood quite well within the framework of standard nebular physics modified to allow for a power law ionizing continuum source (Davidson and Netzer 1979; Kwan and Krolik 1981; Ferland 1981). The

BLR has been found to require densities in excess of  $10^9 \text{ cm}^{-3}$ , certainly precluding forbidden line formation. The necessary incident radiation intensities also require that the majority of the broad-line emission occurs within a few parsecs of the continuum source.

Determining the average conditions for the NLR has been more problematic, and a wide range of densities and ionization parameters has been inferred. Universally, however, the models point to a lower density, a lower radiation intensity, and hence a greater distance for the NLR. Thus, high velocity, high density and small distance are associated with the BLR; the opposite extremes are appropriate for the NLR. This apparent correlation between physical conditions and cloud motion provides both a clue to the correct kinematics and a test for any complete model of the emission line region.

Previous work has focused attention on line intensities or line shapes separately, and then only for the NLR and BLR individually. The above correlation hints that these aspects may not be independent, and the purpose of this work is to investigate their possible relationship. In §II we explore the physical conditions, such as density, column density, and ionization parameter<sup>1</sup> in the NLR by comparing model photo-

---

<sup>1</sup> The ionization parameter  $\Gamma^i$  is differently defined by different authors. We take Kwan and Krolik's definition of  $\Gamma^i = N_{\text{ph}}/N_0$ , i.e. the ratio of ionizing ( $h\nu > 13.6 \text{ eV}$ ) photon density to cloud nucleon density.

---

ionization calculations with a homogeneous set of data. We shall argue that a range of parameters, in particular of density, is required to explain the data. These results will be applied in §III where the consistency of various proposed kinematic models for the BLR will be discussed in the context of their implications for the forbidden line emission. In §IV, sample forbidden line intensities and profiles for a particular kinematic model, the parabolic-orbital model of Kwan and Carroll (1982), will be presented and compared with existing observations.

While this work is primarily concerned with broad line objects (e.g. quasars and Seyfert 1's), we shall also examine various aspects of the narrow line Seyfert 2 galaxies. We do this partly because a large amount of quality data exists, though as yet unanalyzed, partly to help separate the NLR emission from the BLR emission, and partly to contrast the two object classes.

### The NLR Spectrum

We employ a now standard technique to derive typical physical conditions for the NLR by comparing model photoionization calculations with an average observed spectrum. Differences, which are minor, between these and earlier calculations include the use of newer atomic data and a more reasonable input spectrum. Typically, earlier computations have employed a single power law with  $L_\nu \propto \nu^{-1}$  ergs s<sup>-1</sup> Hz<sup>-1</sup>. We here adopt the spectrum assumed in Kwan and Krolik (1981) which

takes into account recent ultra-violet and X-ray continuum observations (Wu et al. 1983; Green et al. 1980) which indicate that the UV index is steeper and the X-ray index less steep than the typical optical index of 1.

These computations also maintain a constant nucleon density throughout the slab. Although constant pressure models may at first seem more "realistic", this is not the case if the ionized gas clouds are confined by an isothermal wind expanding from the continuum source (Krolik et al. 1981; Weymann et al. 1982). In such a case, the wind ram pressure will require a pressure at the illuminated face of the cloud that is twice that at the back. Such a pressure profile is consistent with results of the constant density models where the pressure evaluated at the illuminated surface is more than twice that evaluated at the back.

A more detailed description of the methods, assumptions and data used is given in the Appendix.

A grid of models was computed covering a wide range of nucleon density  $N_0$  and ionization parameter  $\Gamma^i$ . Only models optically thick to the Lyman continuum are considered so that a wide range of ionization level is present in each run. A sharp ionization boundary separates the fully ionized HII region from a partially ionized (electron fraction  $\sim 0.1$ ) zone of indeterminate depth (referred to subsequently as the "extended ionized zone").

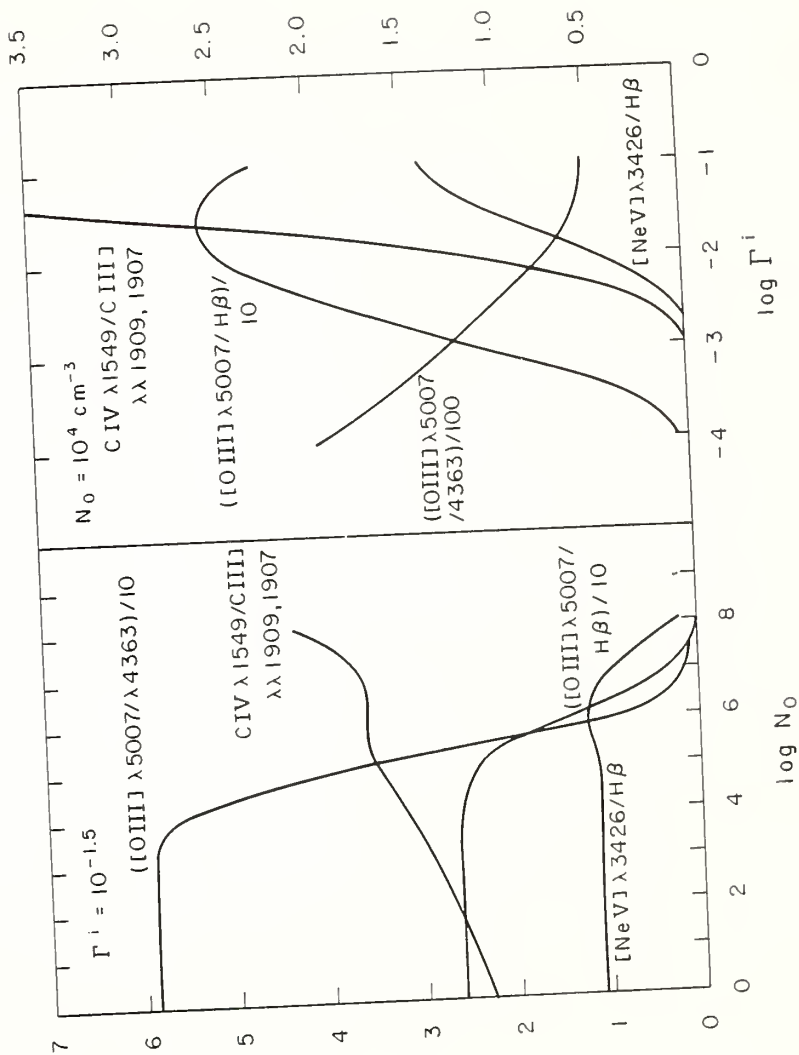
Several line ratios are particularly useful as diagnostics of the physical conditions. Both the [SII] $\lambda 6716/\lambda 6731$  and [OIII] $\lambda 5007/\lambda 4363$



ratios are sensitive to electron density. The former varies from  $\sim 1.5$  at densities  $> 10^2 \text{ cm}^{-3}$  to  $\sim .35$  at densities  $< 10^4 \text{ cm}^{-3}$ . The latter drops from  $\sim 59$  at densities  $< 10^4 \text{ cm}^{-3}$  to near zero at a density of  $\sim 10^7 \text{ cm}^{-3}$ . The  $[\text{OIII}]\lambda 5007/\lambda 4363$  ratio is also a sensitive thermometer at low density, decreasing with increasing temperature from  $\sim 1500$  at  $6000 \text{ K}$  to  $\sim 34$  at  $2 \times 10^4 \text{ K}$ . Raising the ionizing radiation intensity sharply increases both the  $\text{CIV}\lambda 1549/\text{CIII}]\lambda\lambda 1909, 1907$  and  $[\text{NeV}]\lambda 3426/\text{H}\beta$  ratios; these can be used to constrain  $\Gamma^i$ . All but one of these diagnostics are plotted in Figure 4. The left and right panels show the effects of varying  $N_0$  and  $\Gamma^i$  respectively. The plotted lines are produced entirely within the HII zone except for  $\text{H}\beta$  which continues to increase slowly in the extended ionized zone due to recombination, but generally by  $< 10\%$  up to column densities of  $\sim 5 \times 10^{22} \text{ cm}^{-2}$ . For consistency, ratios with  $\text{H}\beta$  are taken at the ionization front boundary (specifically where  $n_{\text{HI}} = n_{\text{HII}}$ ). The  $[\text{SII}]\lambda 6716/\lambda 6731$  ratio is indirectly dependent upon column density since the electron fraction and hence the electron density varies through the extended ionized zone where the  $[\text{SII}]$  emission is produced. For this and other reasons discussed below, a unique curve could not be specified, and so this diagnostic was not plotted. The general nature of the  $[\text{SII}]\lambda 6716/\lambda 6731$  dependence on electron density can be found in Osterbrock (1974).

A large body of high quality data is necessary to obtain a meaningful comparison between model calculations and observations. Despite some progress (Baldwin 1975), the forbidden line data for

Fig. 4. Nucleon density ( $N_0$ ) and ionization parameter ( $\Gamma^i$ ) dependence of several useful diagnostic line ratios. The low density increase in  $\text{CIV}\lambda 1549/\text{CIII}\lambda 1909, 1907$  is due to collisional suppression of the dominant dielectronic recombination process  $\text{C}^{3+} + e^- \rightarrow \text{C}^{2+}$  (see eg. Davidson 1975 and Storey 1981.)



quasars is still rather sparse. A comprehensive program of observation for Seyfert galaxies has been carried out, however, and those observations will provide the necessary data base (Osterbrock 1977; Koski 1978; Shuder and Osterbrock 1981). The great similarity between the Seyfert 1 and quasar broad-line emission is well known, and we will proceed from the assumption that the same processes indeed operate in each, though perhaps on a different luminosity scale. A few quasars will be included so as to support this assumption.

Table 1 presents the average emission line intensities relative to  $[OIII]\lambda 5007$  (single line only) and the diagnostic emission line ratios for the 36 broad-line objects from Osterbrock (1977) (column [1]) and for the 27 Seyfert 2's as identified by Shuder and Osterbrock (1981) (column [2]). The Seyfert 2 spectra are corrected for reddening as described by Koski (1978), while the broad-line objects have no such correction.

In many respects, the narrow line spectrum of Seyfert 1 galaxies resembles that of Seyfert 2's (Osterbrock 1977). The agreement would be closer if some reddening correction were applied to the broad-line data. Arrows show the direction of change for such a correction, and in all cases this is in the right sense. Even so, significant differences remain, especially between the  $[OIII]\lambda 5007/\lambda 4363$  and  $[SII]\lambda 6716/\lambda 6731$  temperature-density diagnostics, as demonstrated by Shuder and Osterbrock (1981). Figure 5 is a two dimensional plot of the histogram pair presented by those authors. This plot shows clearly the distinct segregation between the narrow and broad-line objects

TABLE 1

I/I [OIII] $\lambda$ 5007	RELATIVE INTENSITIES					
	[1]	[2]	[3]	[4]	[5]	[6]
[NeV] $\lambda$ 3426	---	0.10	0.11 $\dagger$	0.04	0.11	0.075
[OII] $\lambda$ 3727	0.21 $\dagger$	0.55	0.11 $\dagger$	0.085	0.03	0.06
[NeIII] $\lambda$ 3869	---	0.16	0.125 $\dagger$	0.07	0.22	0.145
[SII] $\lambda\lambda$ 4069, 4076	---	0.03	----	0.01	0.13	0.07
[OI] $\lambda$ 6300	0.07 $\dagger$	0.06	0.13 $\dagger$	0.12	0.19	0.155
[NII] $\lambda$ 6583	0.56 $\dagger$	0.33	0.34 $\dagger$	0.21	0.215	0.21
[SII] $\lambda\lambda$ 6716, 6731	0.21 $\dagger$	0.16	----	0.145	0.06	0.10
DIAGNOSTIC RATIOS						
[OIII] $\lambda$ 5007/H $\beta$ <sub>nrw</sub>	14.5 <sup>a</sup> 13.5 <sup>b</sup>	10.0	8.9 $\dagger$	26.0	7.3	11.4
[OIII] $\lambda$ 5007/ $\lambda$ 4363	19.3 $\dagger$	48.8	13.4 $\dagger$	59.1	5.0	9.1
[NeV] $\lambda$ 3426/H $\beta$ <sub>nrw</sub>	1.7 <sup>b</sup> $\dagger$	1.2	1.2 $\dagger$	1.1	0.84	0.85
CIV $\lambda$ 1549/CIII] $\lambda\lambda$ 1909,07	---	2.4 <sup>c</sup> $\dagger$	---	3.0	----	----
[SII] $\lambda$ 6716/ $\lambda$ 6731	1.03	1.05	---	1.1	0.35	0.81
[OIII] $\lambda$ 5007/H $\beta$ <sub>tot</sub>	0.48 $\dagger$	----	0.71 $\dagger$	----	----	0.71

## NOTES TO TABLE 1:

Column [1], Seyfert 1's; Column [2], Seyfert 2's; Column [3], quasars; Column [4], model NLR reservoir; Column [5], model infalling cloud system; Column [6], total model spectrum. Arrows show direction of change for reddening correction, and  $\dagger$  means decrease.

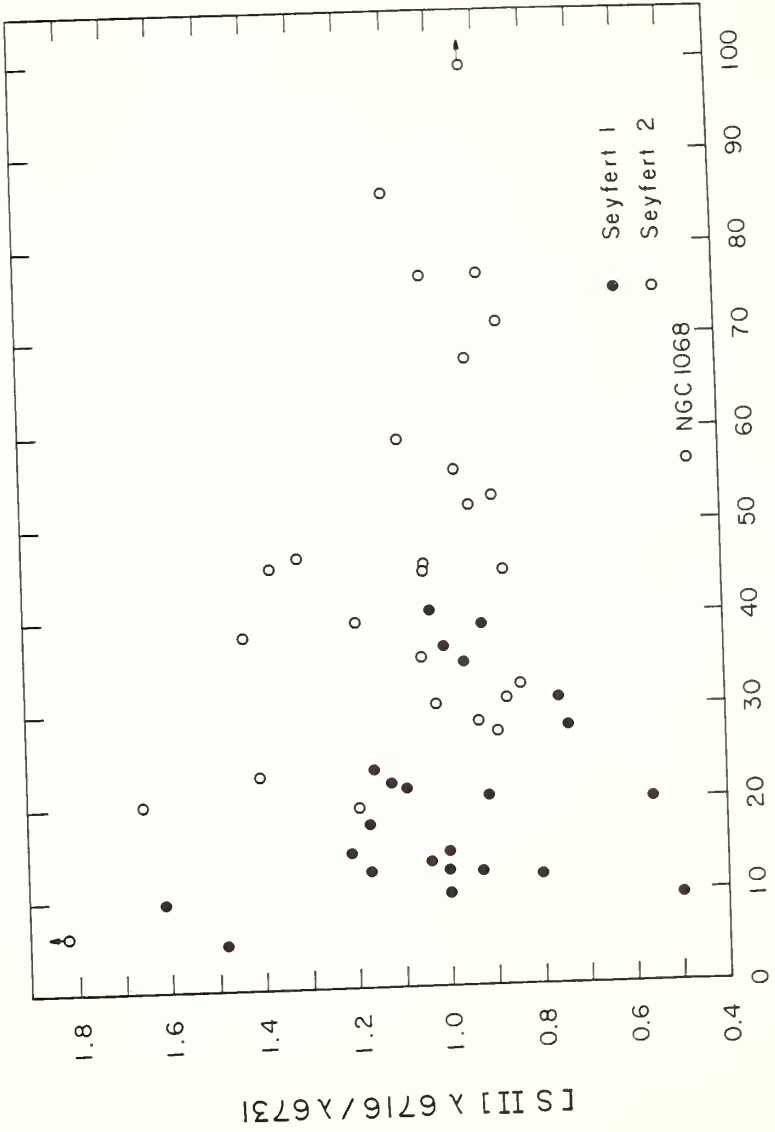
a 3C390.3 BLRG (Netzer 1981) (no reddening correction.)

b NGC4151 (Osterbrock and Koski 1976).

c NGC1068, Mrk 3 (Wu *et al.* 1982) (no reddening correction.)

The bulk of data in Wu *et al.* is for Seyfert 1's and therefore represents the ratio characteristic of the BLR.

Fig. 5. Plot of the density sensitive  $[\text{SII}]\lambda 6716/\lambda 6731$  and temperature - density sensitive  $[\text{OIII}]\lambda 5007/\lambda 4363$  ratios for individual Seyfert 1 (filled circles) and Seyfert 2 (open circles) galaxies. Note that the Seyfert 2 data have been corrected for reddening while the Seyfert 1 data have not. Such a correction would shift the Seyfert 1 points even further to the left of this diagram.



[O III]  $\lambda$  5007 /  $\lambda$  4363

(represented by open and filled circles respectively). Since these line ratios are quite insensitive to reddening, the diagram represents a real difference in physical conditions between the NLR's of these objects. Although the average  $[\text{SII}]\lambda 6716/\lambda 6731$  ratio is the same for both object classes, the broad line objects exhibit much more scatter in this ratio than do the Seyfert 2's. Also, Seyfert 2's cover a broad, continuous range in the  $[\text{OIII}]\lambda 5007/\lambda 4363$  ratio, while the Seyfert 1's tend to cluster at lower values.

The averaged data for 10 quasars from Baldwin (1975) are presented in column (3) of Table 1. No reddening correction has been applied, and, given the small sample, the values are consistent with those for the Seyfert 1's. Unfortunately, the  $[\text{SII}]\lambda 6716/\lambda 6731$  doublet ratio is not available for any of these quasars so they could not be plotted in Figure 2. On the other hand, no quasar has an  $[\text{OIII}]\lambda 5007/\lambda 4363$  ratio greater than 25, and the average value of 13.4 places them securely among the Seyfert 1's.

The base grid point of the photoionization models ( $\Gamma_i = 10^{-1.5}$ ,  $N_o = 10^{3.5} \text{ cm}^{-3}$ ) was chosen to correspond with the typical parameters derived by other authors (Ferland 1981; Netzer 1982). Column (4) lists the line intensities and ratios for this model, which has a total column density of  $5 \times 10^{22} \text{ cm}^{-2}$  (see below for an explanation of this choice). By comparing with the data in columns (1) - (3), several serious deficiencies of this parameter choice are immediately apparent. In particular, the predicted ratios  $[\text{OIII}]\lambda 5007/\lambda 4363 \sim 59$  and  $[\text{OIII}]\lambda 5007/\text{H}\beta \sim 26$  are much too large. The



model predictions can be altered by variation of the standard spectrum, nucleon density, ionization parameter and/or metal abundance. These are discussed in turn below.

A flatter spectrum than that employed would yield a greater heating rate, a greater temperature, and consequently, a smaller  $[OIII]\lambda 5007/\lambda 4363$  ratio. This is in the right direction, but a  $\nu^{-1}$  spectrum only drops the ratio to  $\sim 40$  for the same ionizing photon density (Ferland 1981). Additionally, this would increase the  $[OIII]\lambda 5007/H\beta$  ratio due to the greater required cooling rate.

The effect of adjusting the nucleon density and ionization parameter (on the various diagnostics) can be deduced from Figure 4. Adjustments to the ionization parameter are constrained by the sensitive  $CIV\lambda 1549/CIII]\lambda\lambda 1909, 1907$  and  $[NeV]\lambda 3426/H\beta$  ratios. Unfortunately, only a few observations of each are available. Nevertheless, the two ratios are both consistent with  $\Gamma^i \sim 10^{-1.5}$  and do not allow large deviations from this value. Once again  $[OIII]\lambda 5007/\lambda 4363$  and  $[OIII]\lambda/H\beta$  change in opposite directions and cannot be reduced simultaneously. Also, as seen from Figure 4, the decline in  $[OIII]\lambda 5007/\lambda 4363$  below 50 is very slow with increasing  $\Gamma^i$ . Increasing density suppresses both  $[OIII]\lambda 5007/\lambda 4363$  and  $[OIII]\lambda 5007/H\beta$  while leaving the ionization diagnostics relatively unaffected. A density of  $N_0 > 10^6 \text{ cm}^{-3}$  is necessary, however, and this presents problems by suppressing the  $[SII]\lambda 6716/\lambda 6731$  ratio to  $\sim .35$ .

Decreasing the metal abundance also raises the temperature, this time due to a decreased cooling capacity. Both ratios are reduced,

$[\text{OIII}]\lambda 5007/\lambda 4363$  due to a higher temperature and  $[\text{OIII}]\lambda 5007/\text{H}\beta$  due to the lower oxygen abundance. The base model with heavy elements depleted by a factor of 3 yields  $[\text{OIII}]\lambda 5007/\lambda 4363 \sim 31.8$  and  $[\text{OIII}]\lambda 5007/\text{H}\beta \sim 13.4$ . This seems to be in reasonable agreement with observations until the low ionization lines are considered. Halting integration where  $[\text{OI}]\lambda 6300/[\text{OIII}]\lambda 5007 = .056$ , the average Seyfert 2 value, sets  $[\text{OII}]\lambda 3727/[\text{OI}]\lambda 6300 = .84$  and  $[\text{OII}]\lambda 3727/[\text{NII}]\lambda 6583 = .47$ . The former ratio is 12 times too small and the latter a factor of 3 small. Deeper integration only aggravates the problem. A shallower one, while fixing up these ratios, leaves much too little  $[\text{OI}]\lambda 6300$ , a well determined line. This solution, too, fails.

As none of the above modifications seems satisfactory, we are led to consider the next simplest case of a two component NLR. Koski (1978) has nicely demonstrated the correlations among the intensities of low ionization lines on the one hand and those among high ionization lines on the other. Also noting that the two groups were uncorrelated with each other, Koski suggested the presence of two independent ionization zones, one for each ionization group. While this effect could, in isolation, be explained by means of an independently varying cloud column density, the intensity and line ratio problems discussed above force consideration of two separate cloud systems of predominantly high and low ionization respectively. Netzer (1982) came to the same conclusion for 3C390.3.

The extra freedom allowed by a two component model weakens the constraints which can be imposed in selecting the "correct" set of

cloud conditions. Many possible combinations of the above parameters could yield satisfactory spectra in agreement with the data. The simplest solution, however, would be a straight forward variation in cloud density as follows: 1) to suppress the [OIII] ratios, the high ionization lines are formed predominantly at high density ( $N_O > 10^6 \text{ cm}^{-3}$ ) with a typical ionization parameter  $\Gamma^i = 10^{-1.5}$ , and 2) a region of lower density wherein much of the [SII], [OII], [OI] and [NII] emission is produced. The [SII] $\lambda$ 6716/ $\lambda$ 6731 ratio sets this cloud density close to  $N_O \sim 10^{3.5} \text{ cm}^{-3}$ .

Given  $\Gamma^i$  and  $N_O$  for the various emission-line regions, namely the BLR and the high and low density NLR components, it is easy to determine the positional relationships among them. For an unattenuated point source of continuum radiation,  $N_O \Gamma^i \propto r^{-2}$  from that source. Using the BLR parameters of  $\Gamma^i = 10^{-1.5}$  and  $N_O = 4 \times 10^9 \text{ cm}^{-3}$  for a typical quasar (Kwan and Krolik 1981), we find that the high density component of the NLR ( $\Gamma^i = 10^{-1.5}$ ,  $N_O = 10^6$ ) is about 63 times and the low density component ( $\Gamma^i = 10^{-1.5}$ ,  $N_O = 10^{3.5}$ ) about  $1.1 \times 10^3$  times further away from the radiation source. Since the typical BLR size is 1 pc, those numbers are also the radial distances in parsecs from the quasar center.

Figures 6 and 7 display the density dependence of the major forbidden line intensities relative to H $\beta$ . All curves were computed for a constant ionization parameter  $\Gamma^i = 10^{-1.5}$ , and integration was stopped at a nucleon column density of  $N_C = 5 \times 10^{22} \text{ cm}^{-2}$ . At this depth, the temperature and electron fraction are  $< 8500 \text{ K}$  and  $< 0.1$  respectively,

Fig. 6. Nucleon density dependence of the total line emission relative to  $H\beta$  for various lines formed in the fully ionized HII zone.

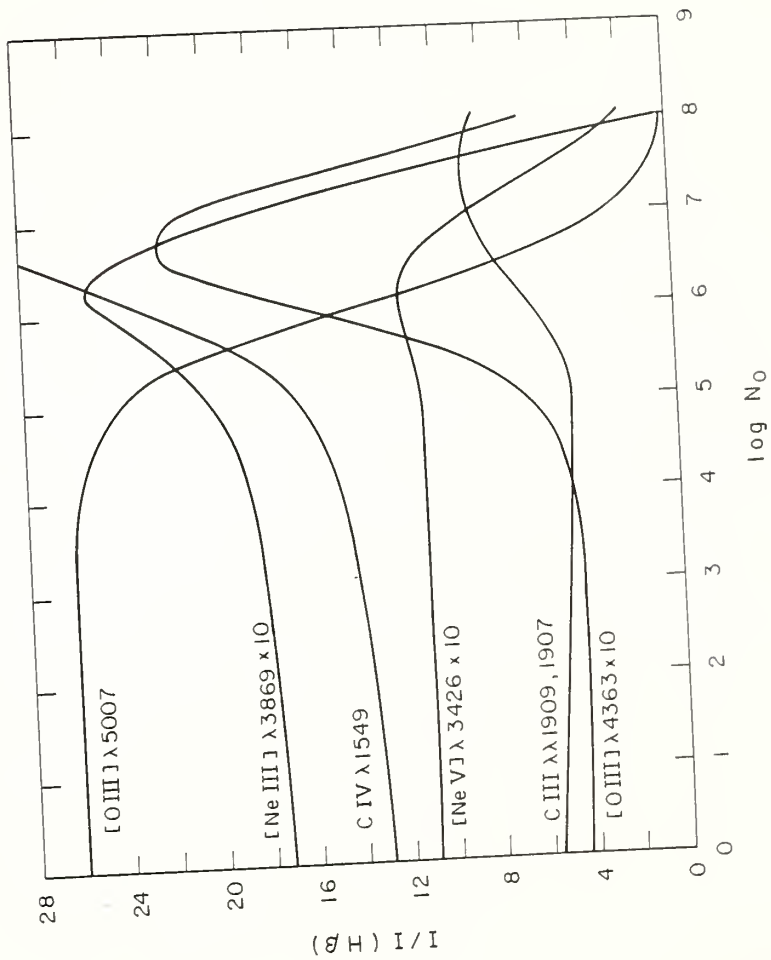
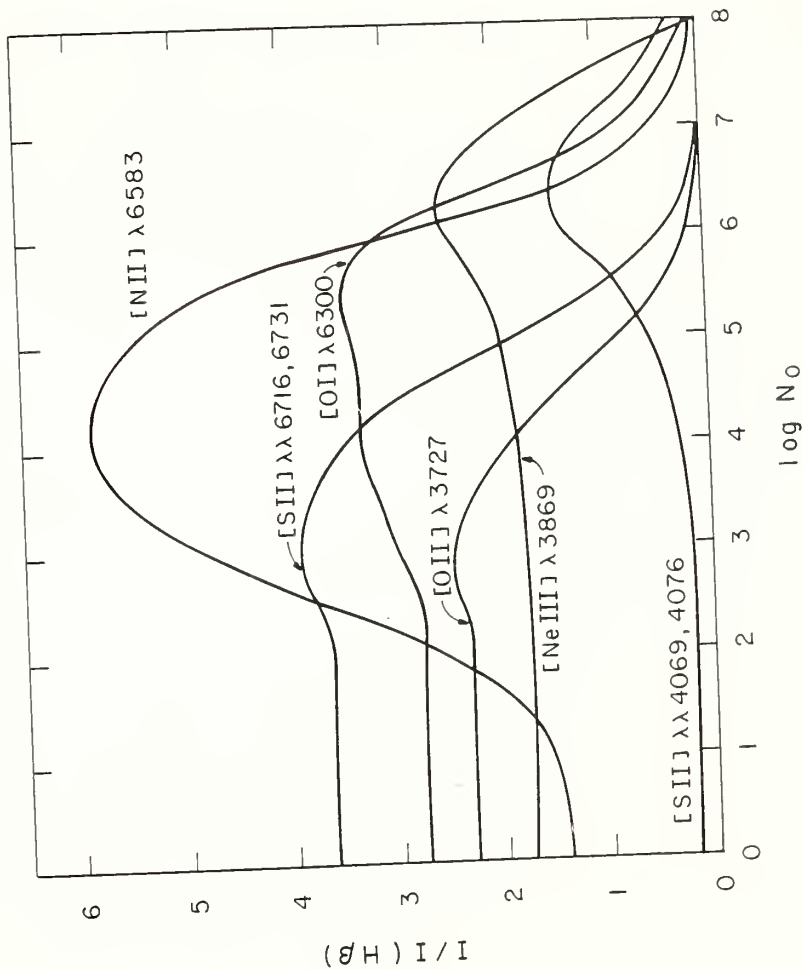


Fig. 7. As in Fig. 6 except that lines produced in the extended ionized zone are plotted. The initial large increase in  $[\text{NII}]\lambda 6583/\text{H}\beta$  with rising density is due to the increasing ionization of NI from its excited  $2D$  state as that state becomes more fully populated.



and only slow increases in  $[OI]\lambda 6300$ ,  $[NII]\lambda 6583$ , and  $[SII]\lambda\lambda 6716, 6731$  are obtained by further integration. The particular choice for  $N_c$  is determined by the following dynamical consideration.

All models of the emission line region require that the broad-line clouds be confined by the pressure of a hot tenuous external medium. Recent work (Krolik et al. 1981; Weymann et al. 1982) indicates that this intercloud medium has a temperature exceeding  $10^8$  K and is most likely in expansion. Such an isothermal wind will drag on the NLR clouds, producing an acceleration  $a_{\text{drag}} = p_w / (N_c m_H)$ , with  $p_w$  the wind pressure, and  $m_H$  the mass of hydrogen. Numerically,

$$p_w \sim 4 \times 10^{13} \text{ k} \left( \frac{1 \text{ pc}}{r} \right)^2 \text{ erg cm}^{-3},$$

assuming that the BLR clouds, with a density of  $10^9 \text{ cm}^{-3}$  at 1 pc and a temperature of  $2 \times 10^4$  K, are in pressure balance with the wind. To resist this outward acceleration, orbiting NLR clouds must be bound such that  $N_c$  and the mass interior to the NLR satisfy  $N_c M > 2.5 \times 10^{32} M_\odot \text{ cm}^{-2}$ . A value of  $M = 5 \times 10^9 M_\odot$  is consistent with narrow line widths of  $\sim 100 - 700 \text{ km s}^{-1}$  at 60 - 1000 pc if these are indeed due to orbital motion. This mass implies cloud column densities  $N_c > 5 \times 10^{22} \text{ cm}^{-2}$ , which we adopt for want of a better justified value.

While we could now synthesize a total narrow line spectrum from the best fit parameters for each component, considerations of dynamics in section III suggest a realistic generalization of the above simplistic model. This modification envisages a range of cloud den-



ities rather than two discrete values. Since the exact nature of the density variation depends upon the particular kinematic model employed, we defer until section IV the presentation of calculated narrow line intensities and profiles for a particular model, and discuss first, in the next section, the implications for the forbidden line emission of the various proposed BLR kinematic models.

### Broad-Line Kinematic Models and the Associated Forbidden Line Emission

Three distinct physical mechanisms have been proposed to explain the origin of the broad-line cloud velocities. These are radiative acceleration (Blumenthal and Mathews 1975; Mathews 1982), ballistic outflow (Capriotti, Foltz, and Byard 1980) and gravitational infall (Kwan and Carroll 1982). Each process has some incidental consequences for the forbidden line emission which need to be considered for a consistent model of the broad and narrow emission line regions.

One constraint on the NLR gas applies to the radiative acceleration model in particular. For an optically thick cloud, the radiative acceleration is

$$a_{\text{rad}} = \frac{L_{\text{ion}}}{4\pi r^2 c} \frac{1}{N_c m_H} = \frac{2 N_o \Gamma^1}{N_c m_H}$$

where  $L_{\text{ion}}$  is the ionizing ( $h\nu > 13.6$  eV) photon luminosity. This acceleration must dominate gravity by a large amount. Since both radiation pressure and gravitational attraction fall off as  $r^{-2}$ , NLR

clouds will be accelerated at the same time as broad-line clouds of similar column density. If the broad-line clouds ( $\Gamma^i = 10^{-1.5}$ ,  $N_o = 4 \times 10^9 \text{ cm}^{-3}$ ) accelerate to speeds of  $\sim 10^4 \text{ km s}^{-1}$ , then the high and low density narrow-line clouds ( $\Gamma^i = 10^{-1.5}$ ,  $N_o = 10^6 \text{ cm}^{-3}$ , and  $\Gamma^i = 10^{-1.5}$ ,  $N_o = 10^{3.5} \text{ cm}^{-3}$ ) will attain velocities of  $\sim 1.3 \times 10^3 \text{ km s}^{-1}$  and  $\sim 300 \text{ km s}^{-1}$  respectively. Either the narrow-line clouds have column densities considerably greater than those of the BLR clouds, or they must be continually replenished. This replenishment cannot occur via the BLR since those outflowing clouds have velocities  $> 10^4 \text{ km s}^{-1}$ , and the associated mass loss rate is much too small. This problem could be avoided if considerable mass lies between the BLR and NLR proper.

All three models have been proposed to explain the logarithmic line shape observed in the wings of the broad permitted lines. Given the freedom of choice for parameters, all are reasonably successful. The broad-line clouds will also contribute to the forbidden line emission during the course of their motion as they continually adjust to the external pressure. This associated forbidden line emission will have intensities and profiles dependent upon the particular kinematic model, and their comparison with observations can provide a useful test for the models.

The integrated emission ( $\text{ergs s}^{-1}$ ) of a line can be written, for a spherically symmetric flow, as:

$$L_{\text{line}} = 4\pi \int_{r_1}^{r_2} n_c \epsilon_{\text{line}} r^2 dr \quad (\text{III-1})$$

where  $n_c$  is the cloud number density and  $\epsilon_{\text{line}}$  is the line luminosity of a single cloud. We assume a steady mass flow so that

$$n_c = \frac{\dot{M}}{4\pi r^2 v M_c}$$

with  $v$  the cloud velocity,  $\dot{M}$  the mass flow rate, and  $M_c$  the cloud mass. If all line emission is normalized to that of H $\beta$ , the luminosity of any line can be written as:

$$L_{\text{line}} = \frac{\dot{M}}{M_c} \int_{r_1}^{r_2} \frac{\epsilon_{\text{H}\beta}}{v} R_{\text{line}}(r) dr \quad (\text{III-2})$$

where  $R_{\text{line}}(r) = \epsilon_{\text{line}}/\epsilon_{\text{H}\beta}$ .

In the radiative and ballistic outflow models, the broad-line clouds, as they move away from the central source, will expand in size owing to the decreasing external pressure. When the density within the cloud decreases sufficiently, forbidden line emission will become effective. By this time the clouds will have attained their maximum velocity so that  $v = \text{constant} = v_{\text{max}}$  in eq. (III-2). Also, these clouds will eventually become optically thin to the Lyman continuum since the column density  $N_c \sim r^{-4/3}$  as they expand with the wind. The maximum fully ionized column density is  $\sim \Gamma^i c/\alpha_B \sim 3.6 \times 10^{21} \text{ cm}^{-2}$ , where  $\alpha_B$  is the case B recombination coefficient and  $\Gamma^i$  is taken to be  $10^{-1.5}$ . Taking  $N_c \sim 5 \times 10^{22} \text{ cm}^{-2}$  as a representative value at 1 pc, a cloud will become optically thin at  $\sim 7.2$  pc with a corresponding cloud density of  $2 \times 10^7 \text{ cm}^{-3}$  (assuming  $N_o = 10^9 (1 \text{ pc}/r)^2 \text{ cm}^{-3}$ ).

When a cloud is optically thin, the H $\beta$  emission is  $\epsilon_{\text{H}\beta} = N_o \alpha_{\text{H}\beta} h\nu_{\text{H}\beta} M_c/v_{\text{H}}$  with  $\alpha_{\text{H}\beta}$  the effective recombination coef-

ficient for the production of H $\beta$ . With a cloud density parameterized as  $N_0 = 10^9 (r_0/r)^2 \text{ cm}^{-3}$  and the above emissivity, a variable change transforms eq. (III-2) to:

$$L_{\text{line}} = \alpha_{\text{H}\beta} h\nu_{\text{H}\beta} \frac{\dot{M}}{m_{\text{H}}} \frac{10^{4.5} r_0}{2 v_{\text{max}}} \int_0^{10^8} R_{\text{line}}(N_0) \frac{d N_0}{N_0^{1/2}} \quad (\text{III-3})$$

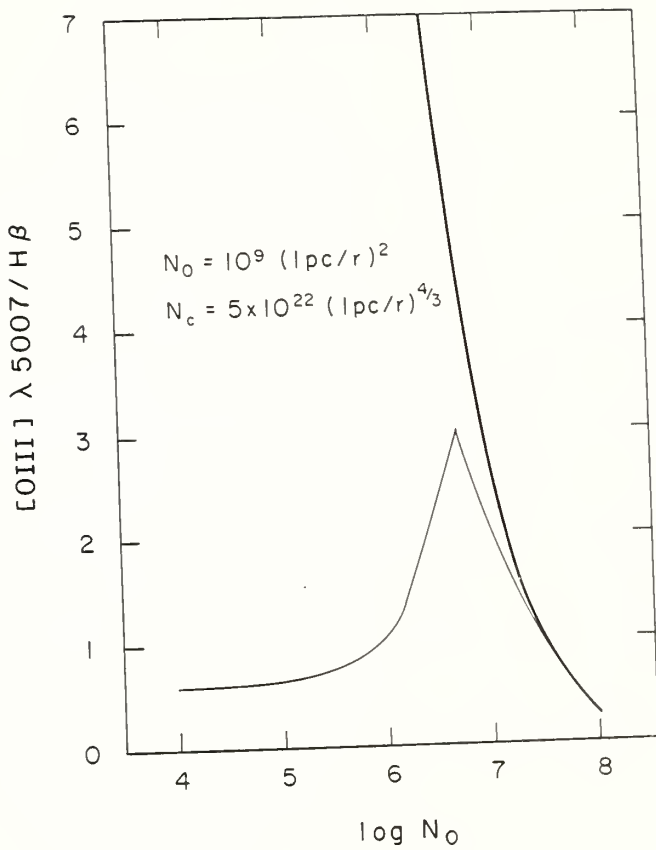
The upper integration limit of  $N_0 = 10^8 \text{ cm}^{-3}$  is taken since at higher densities  $R_{\text{line}}$  is effectively zero for all of the forbidden lines of interest (c.f. Figs. 6 and 7).

The forbidden line of most interest is [OIII] $\lambda$ 5007 because of its great observed strength. The critical density for collisional de-excitation of this line is  $\sim 10^6 \text{ cm}^{-3}$  (c.f. Fig. 6), so that by the time emission of this line becomes effective in the outflow models, the clouds will have become optically thin to the Lyman continuum. The density dependence of  $R_{5007}$  in Figure 6 is not appropriate for optically thin clouds since, as the cloud column density decreases, part of the [OIII] zone is truncated and its emission thereby reduced. Figure 8 displays the line emission relative to H $\beta$  for a cloud with density

$$N_0 = 10^9 \left( \frac{1 \text{ pc}}{r} \right)^2 \text{ cm}^{-3} \text{ and column density } N_c = 5 \times 10^{22} \left( \frac{1 \text{ pc}}{r} \right)^{4/3} \text{ cm}^{-2}.$$

We see that  $R_{5007} < 3$  for all  $N_0$ . Performing the integral over  $R_{5007}$  numerically, eq. (III-3) yields for the associated [OIII] $\lambda$ 5007 emission

Fig. 8. The density dependence of the total [OIII] $\lambda$ 5007 emission relative to that of H $\beta$  is plotted for the case of an optically thick cloud (thick line) and for a cloud which becomes optically thin to Ly $\alpha$  at a density  $N_0 \sim 2 \times 10^7 \text{ cm}^{-3}$ . The listed radial dependences of  $N_0$  and  $N_c$  are appropriate for a spherically expanding cloud.  $\Gamma^i = 10^{-1.5}$  is assumed.



from the broadline clouds:

$$L_{5007} = 10^{8.2} \frac{\dot{M}}{m_H} \frac{r_0}{v_{\max}} \alpha_{H\beta} h\nu_{H\beta} .$$

The BLR contribution to H $\beta$  for the radiative acceleration model is obtained by substituting  $dr = 4\pi r^2 c M_C v dv / (A_C L_{\text{ion}})$  and  $\epsilon_{H\beta} = (A_C / 4\pi r^2) (\alpha_{H\beta} \nu_{H\beta} / \alpha_B \bar{\nu}) L_{\text{ion}}$ , appropriate expressions for optically thick clouds, into eq. (III-2). Here  $A_C$  is the cloud area and  $\bar{\nu}$  the mean energy of ionizing photons with energy  $< 54.4$  eV. This gives:

$$L_{H\beta} = \dot{M} c \frac{\alpha_{H\beta} \nu_{H\beta}}{\alpha_B \bar{\nu}} \int_{v_{\min}=0}^{v_{\max}} dv = \dot{M} c \frac{\alpha_{H\beta} \nu_{H\beta}}{\alpha_B \bar{\nu}} v_{\max} . \quad (\text{III-4})$$

This total represents emission due to recombination only and must be multiplied by a factor  $\sim 5$  to account for collisional production of H $\beta$  (Kwan and Krolik 1981). Relative to H $\beta$ , the associated [OIII] $\lambda 5007$  emission from the broad-line clouds is then:

$$\frac{L_{5007}}{(L_{H\beta})_{\text{Brd}}} = \frac{10^{8.2} r_0 \alpha_B h\bar{\nu}}{5 c m_H v_{\max}^2} = .017$$

evaluated for  $r_0 = 1$  pc,  $h\bar{\nu} = 21.7$  eV, and  $v_{\max} = 10^4$  km s $^{-1}$ . Similar results are obtained for the ballistic outflow model. If a great amount of X-ray radiation contributes to acceleration of the cloud, then this result must be multiplied by a factor  $L_{\text{ion}}(< \nu_X) / L_{\text{ion}}(< 54.4 \text{ eV}) \sim 3$  for  $\nu_X = 10$  keV.

The observations (c.f. Table 1) indicate that  $[OIII]\lambda 5007 / (H\beta)_{Brd} > 0.5$  for broad-line objects. We therefore conclude that an outflowing BLR contributes negligibly to the total  $[OIII]\lambda 5007$  emission. If somehow detectable, this contribution would manifest itself as a weak broad component with a rectangular profile extending to  $v_{max}$ . Other forbidden lines would exhibit components with this same shape and width, but these too would be very weak.

Broad-line clouds originating by gravitational infall will contribute to the forbidden line emission in a different way. In this case, clouds remain optically thick for all densities during the infalling leg. Using  $v = (2 GM_Q/r)^{1/2}$ , with  $M_Q$  the quasar central mass, and  $R_{5007}(N_O)$  from Figure 6, the  $[OIII]\lambda 5007$  luminosity from the infalling clouds is:

$$L_{5007} = 1.2 \times 10^2 \frac{\dot{M}}{M_c} \frac{A_c L_{ion}}{10^{9/4} r_o^{1/2} (2GM_Q)^{1/2}} \frac{\alpha_{H\beta} v_{H\beta}}{\alpha_B \bar{v}},$$

where the integration over  $R_{5007}$  has been performed numerically. The broad  $H\beta$  luminosity is:

$$(L_{H\beta})_{Brd} = \frac{5}{4\pi} \frac{\dot{M}}{M_c} \frac{A_c}{GM_Q} \frac{\alpha_{H\beta} v_{H\beta}}{\alpha_B \bar{v}} L_{ion} v_{max}$$

so that the relative broad-line contribution to  $[OIII]\lambda 5007$  during the infalling leg will be:



$$\frac{L_{5007}}{(L_{H\beta})_{\text{Brd}}} = \frac{151}{10^{9/4}} \frac{(2GM_Q/r_0)^{1/2}}{v_{\text{max}}} = 0.51$$

evaluated for  $r_0 = 1$  pc,  $M_Q = 5 \times 10^9 M_\odot$  and  $v_{\text{max}} = 10^4$  km s $^{-1}$ . In the outward leg of the parabolic-orbital model, the H $\beta$  emission is nearly equal to that in the inward leg. The [OIII] $\lambda$ 5007 emission, however, is much smaller since the clouds will now be accelerated by the quasar wind and become optically thin by the time the [OIII] $\lambda$ 5007 emission becomes effective.

It is clear that broad-line clouds in a gravitational infall model will necessarily produce significant emission in [OIII] $\lambda$ 5007 and other forbidden lines. This has been previously pointed out by Shields (1978). Detailed profiles and intensities depend on the particular density dependence of each line, but some general trends can be noted. Most importantly, the width of this forbidden line component will correspond to that velocity at which the cloud density exceeds the line's critical density for collisional de-excitation. With critical densities determined from Figures 6 and 7, the forbidden line emission from the infalling clouds will have different widths increasing in the order [OII] $\lambda$ 3727 < [SII] $\lambda$  $\lambda$ 6716, 6731 < [NII] $\lambda$ 6583 < [OIII] $\lambda$  $\lambda$ 007 < [OI] $\lambda$ 6300 < [NeIII]  $\lambda$ 3869 < [NeV] $\lambda$ 3426. These widths, however, will all be significantly less than those of the permitted lines.

There are some indications that the above trends agree with observations. Recent high resolution analysis of [OIII] $\lambda$ 5007 line profiles (Pelat and Alloin 1980, 1982) has revealed a broad component of comparable intensity to the narrow core, and that the width of this com-

ponent is much less than that of the permitted lines. Evidence also exists for line width differences among the various forbidden lines. Phillips (1976) has noted for I Zw 1 that the [OIII] and [NeIII] lines are broader than the lower ionization lines. Ward (1978) has made a detailed study of NGC 3783 and demonstrated a hierarchy of line widths such that lines are broader for ions with higher ionization potentials. The observation has also been made that generally [NeV] $\lambda$ 3426 is broader than [OIII] $\lambda$ 5007 in quasars (Pelat et al. 1981). It is important to note that the ionization potential ordering OI < SII < NII < OII < OIII < NeIII < NeV is also roughly the ordering of critical density, and we suspect that the true correlation is between critical density and velocity. In any case, a gravitational infall model appears more easily reconcilable with these data than do outflow models.

In section II, we found that the narrow-line emission most likely consists of at least two cloud systems, a high density component and a low density component respectively. Considering the previous discussion, a straight-forward generalization of this simple two-component NLR model is that the high density component comprises a continuous range of densities and velocities. This picture fits nicely into the kinematic model proposed by Kwan and Carroll (1982). In that picture, clouds in a distant reservoir are perturbed into highly eccentric orbits which feed into the BLR. Confined and compressed by the quasar wind, these clouds increase in both density and velocity toward the quasar center. This intermediate zone between the reservoir and the BLR proper constitutes the high density NLR component. The

model as proposed considered a return journey after the clouds reach periastron, but the forbidden line emission associated with that outward leg, just as in the case of pure outflow, is negligible. Predicted profiles and intensities for the parabolic-orbital model are presented in the next section.

### Model Profiles and Intensities

Individual line profiles and intensities were computed with the parabolic-orbital kinematic model of Kwan and Carroll (1982) by incorporating the density dependent emissivities depicted in Figures 6 and 7. A central mass of  $5 \times 10^9 M_{\odot}$  and a cloud density  $N_0 = 10^9 (1 \text{ pc}/r)^2 \text{ cm}^{-3}$  were assumed. This places the NLR reservoir at a distance of 560 pc and with an orbital velocity of  $250 \text{ km s}^{-1}$ . A  $r^{-2}$  density dependence also guarantees that  $\Gamma^i$  remains constant as a cloud falls in. Infalling clouds that will eventually produce broad-line emission were given an average angular momentum of  $4000 \text{ km s}^{-1} \times \text{pc}$  with a range between 2000 and  $6000 \text{ km s}^{-1} \times \text{pc}$ ; the results are quite insensitive to this choice since the forbidden line emission occurs while the cloud motion is essentially radial.

Each line profile is the sum of two parts, one part being contributed by the NLR reservoir and the other part by the infalling clouds. The NLR spectrum for  $N_0 = 10^{3.5}$  and  $\Gamma^i = 10^{-1.5}$  is listed in column [4] of Table 1. The integrated emission of the infalling cloud system is given in column [5]. The resultant total spectrum was obtained by

requiring that the NLR reservoir and the infalling cloud system contribute equally to the total  $[\text{OIII}]\lambda 5007$  intensity. This is consistent with the gaussian decompositions of the observed emission by Pelat and Alloin (1980, 1982). The resultant spectrum appears in column [6].

The two ratios of  $[\text{OIII}]\lambda 5007$  and  $[\text{NeV}]\lambda 3426$  to  $\text{H}\beta_{\text{nrw}}$  listed in Table 1 require special mention. When these ratios are derived observationally, only the central narrow component of  $\text{H}\beta$  is supposedly considered; typically this is deduced to be  $< 20\%$  of the total  $\text{H}\beta$  emission. In our synthetic spectrum, the contribution of the NLR reservoir to the total  $\text{H}\beta$  emission is only  $\sim 1\%$ , while the infalling cloud system, during the course of motion between the NLR reservoir and 3 pc, contributes another 5%. The significant contribution to the  $\text{H}\beta$  profile from a continuous range of velocities in a gravitational infall model makes it difficult to define and extract a unique "narrow component". Table 2 shows, for the numerical model, the integrated emission (in arbitrary units) of  $\text{H}\beta$  and  $[\text{OIII}]\lambda 5007$  from essentially infinity to various distances from the quasar center. The infall velocity at each point is also indicated. The observationally derived  $[\text{OIII}]\lambda 5007/(\text{H}\beta)_{\text{nrw}}$  ratio will clearly depend on the velocity width attributed to the assumed narrow  $\text{H}\beta$  component as well as on the care with which the  $[\text{OIII}]\lambda 5007$  wings are being measured. With no better choice in sight, we determine reasonable lower limits to the  $[\text{NeV}]\lambda 3426/(\text{H}\beta)_{\text{nrw}}$  and  $[\text{OIII}]\lambda 5007/(\text{H}\beta)_{\text{nrw}}$  ratios by taking  $(\text{H}\beta)_{\text{nrw}}$  to be that  $\text{H}\beta$  emission formed beyond 3 pc from the quasar center. This

TABLE 2  
INTENSITIES

r (pc)	v (km s <sup>-1</sup> )	H $\beta$	[OIII] $\lambda$ 5007	[OIII] $\lambda$ 5007/H $\beta$
>100	600.	7.42	189.	25.5
>30	1070.	18.6	405.	21.8
>10	1900.	40.3	518.	12.9
>3	3370.	78.0	570.	7.3

distance was chosen because within it the  $[OIII]\lambda 5007$  and  $[NeV]\lambda 3426$  emission is negligible. These are the ratios which appear in column [5] of Table 1.

The ratio  $[OIII]\lambda 5007/H\beta_{tot}$  is also given in column [6].  $H\beta_{tot}$  includes a factor of 5 for collisional production of  $H\beta$  in the BLR, a factor of 2 for the return leg emission, and assumes a cloud area  $A_c = \text{constant}$  for  $r > 1$  pc, and  $A_c \propto r^{4/3}$  for  $r < 1$  pc. For a strictly constant cloud area,  $[OIII]\lambda 5007/H\beta_{tot} = 0.37$ .

The total spectrum is a reasonable fit to the observed one. The most important success is the resolution of the  $[OIII]$  problem. The  $[OIII]\lambda 5007/H\beta_{nrw}$  and  $[OIII]\lambda 5007/\lambda 4363$  ratios can be adjusted up or down by changing the relative contribution of the infalling component, while leaving the  $[SII]\lambda 6716/\lambda 6731$  ratio basically unchanged. Thus the variation in the  $[OIII]\lambda 5007/\lambda 4363$  ratio in Figure 5 can be explained as due to a varying amount of infalling gas. Values of  $[OIII]\lambda 5007/\lambda 4363 > 50$  would preclude any significant amount of infalling gas at all. This would apply to most Seyfert 2's and would be consistent with the weakness or complete lack of any permitted line BLR in these objects.

Except for  $[OI]\lambda 6300$  and  $[OII]\lambda 3727$ , the calculated and observed strengths of most lines agree to better than 50%. The former is computed to be about twice as strong as observed. A considerable fraction of its emission occurs in broad wings, however, and may have been missed amidst the noise in previous observations. It is suggested that a careful subtraction of the continuum would reveal extended emission

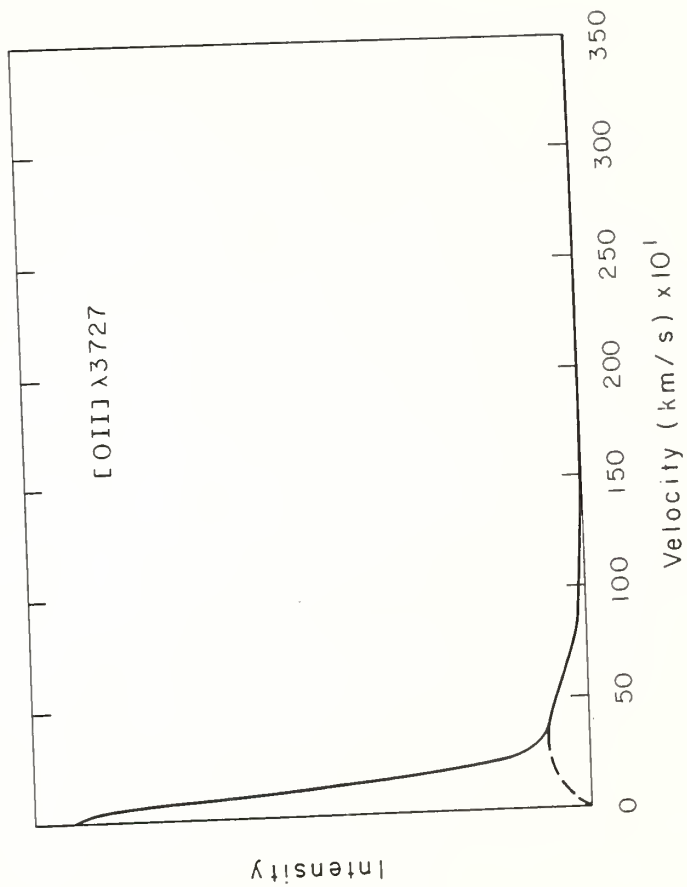
in [OI] $\lambda$ 6300 and other weak forbidden lines. The observed strength of [OII] $\lambda$ 3727, especially in Seyfert 2's, would seem to require an additional region of very low ionization such that [OII] $\lambda$ 3727/[OIII] $\lambda$ 5007 is large there. Such a source could be galactic HII regions for example.

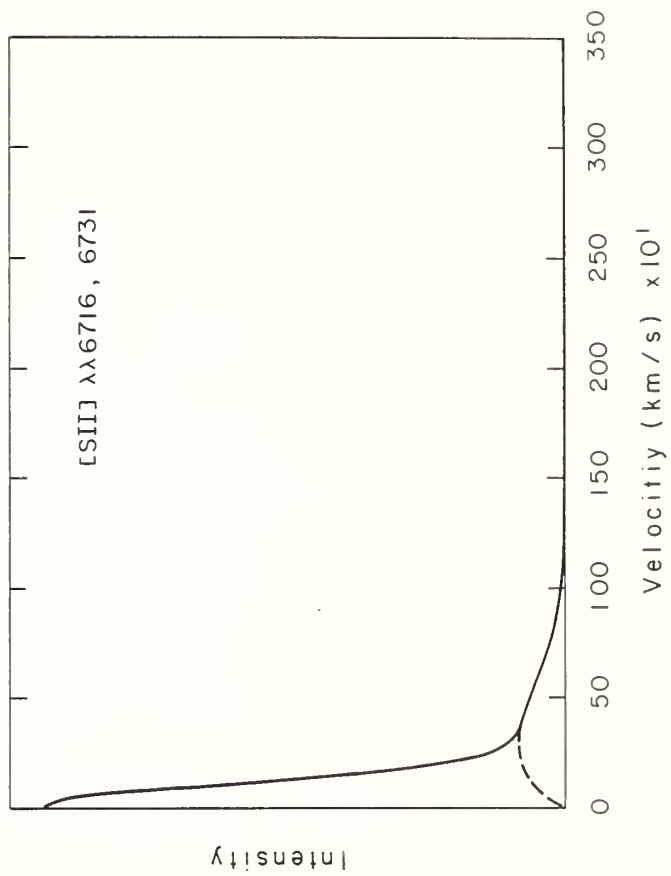
The profiles of all forbidden lines considered are presented in Figure 9 in order of increasing FWZI. These were generated by adding the computed line profile from the infalling cloud system to a gaussian component of FWHM = 250 km s<sup>-1</sup> which represents the emission profile from the NLR reservoir. The relative strength of each component was determined by its contribution to the total spectrum discussed above. A wide range of line widths is present, and the ordering agrees with the expected trends as discussed in section III. The [OIII] $\lambda$ 4363 and [SII] $\lambda$ 4069,4076 lines have substantial broad emission since those lines arise from excited ionic states which are more fully populated at high density.

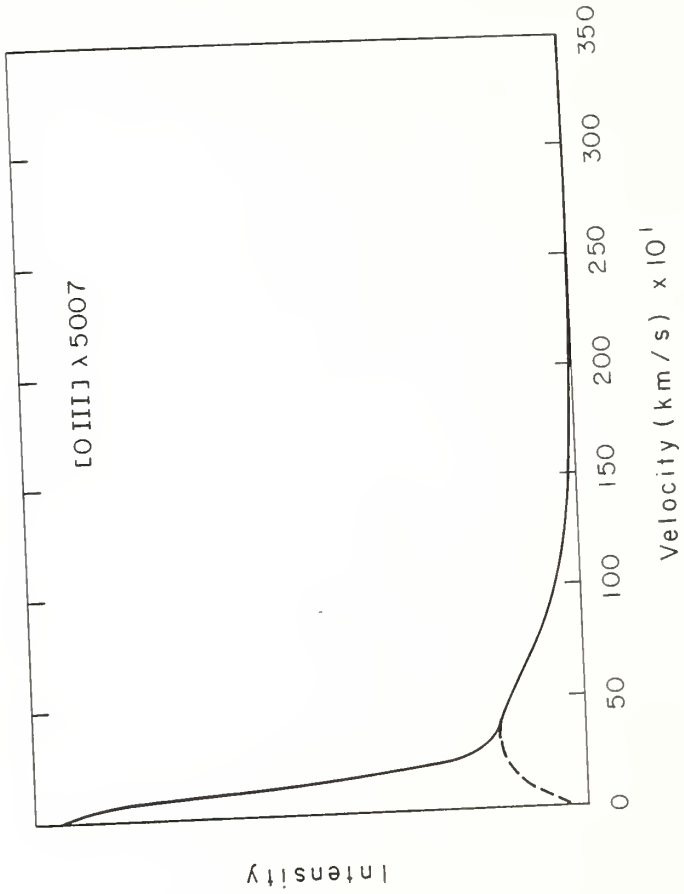
The model forbidden line profiles, as presented, are completely symmetric about the line center. High resolution observations of the [OIII] $\lambda$ 5007 profile in Seyfert galaxies (Heckman et al. 1981) indicate that, in general, the emission is stronger in the blue wing than in the red. This effect, however, is not as pronounced for quasars as it is for the Seyfert galaxies (Miley and Heckman 1982). This observed asymmetry is easily accommodated within the present model. Emitting clouds with a mixture of dust will preferentially emit [OIII] $\lambda$ 5007 from their illuminated face due to absorption by dust in the back of the cloud.

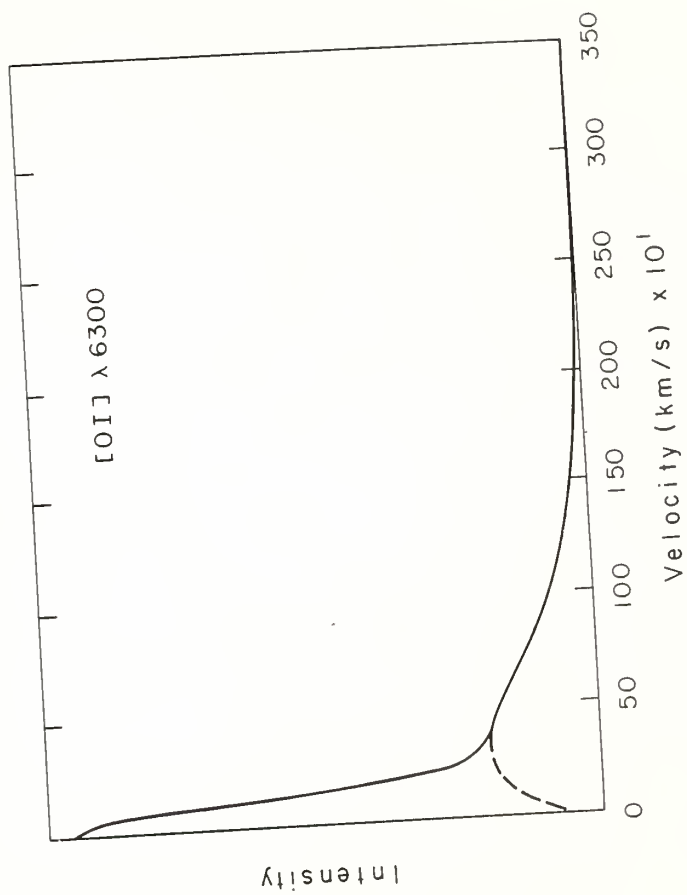
Fig. 9. Synthetic line profiles are given in order of increasing FWZI. Dashed lines show the emission from the infalling leg alone.

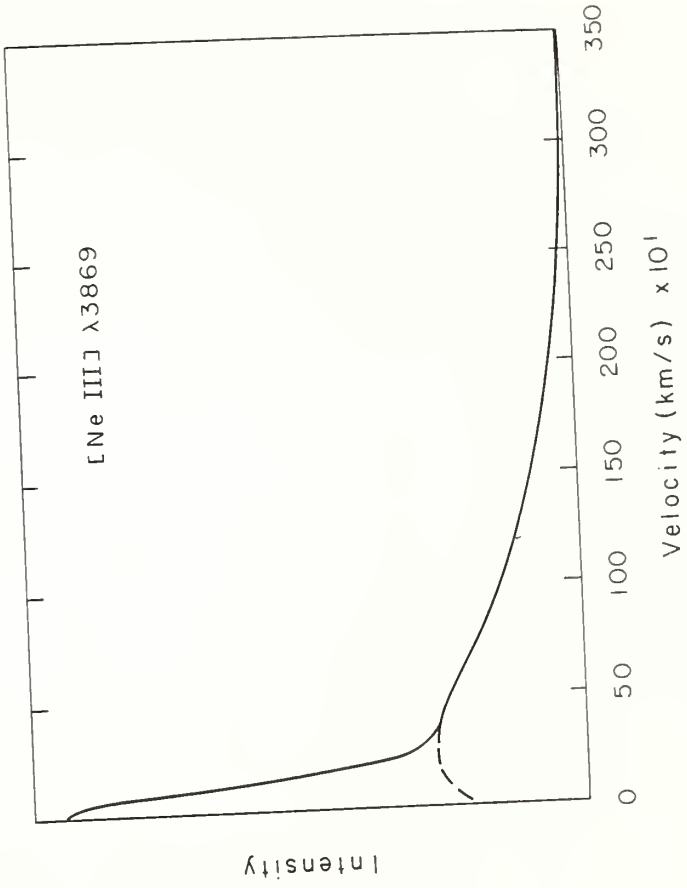


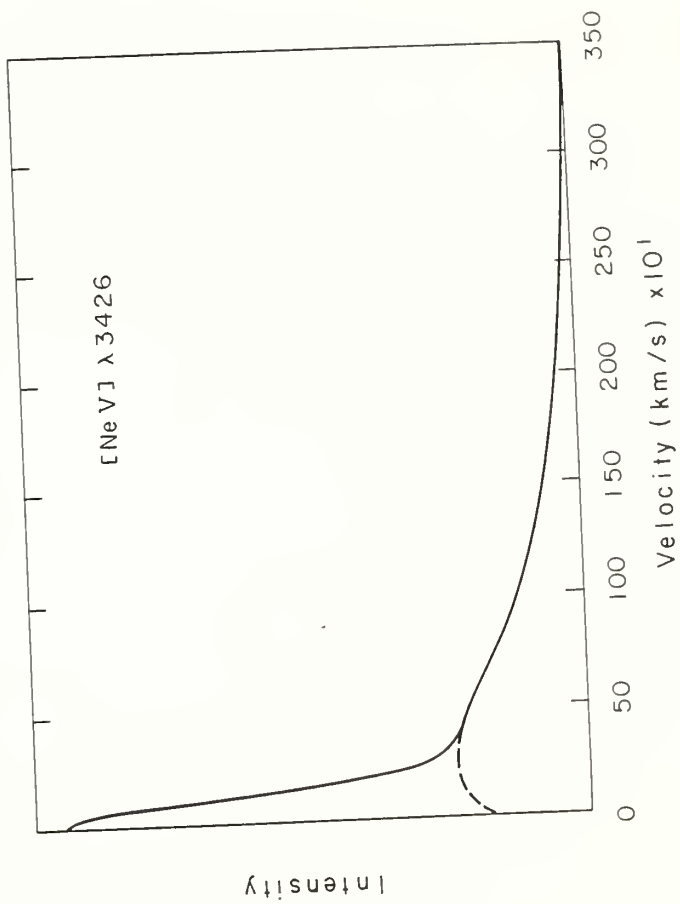


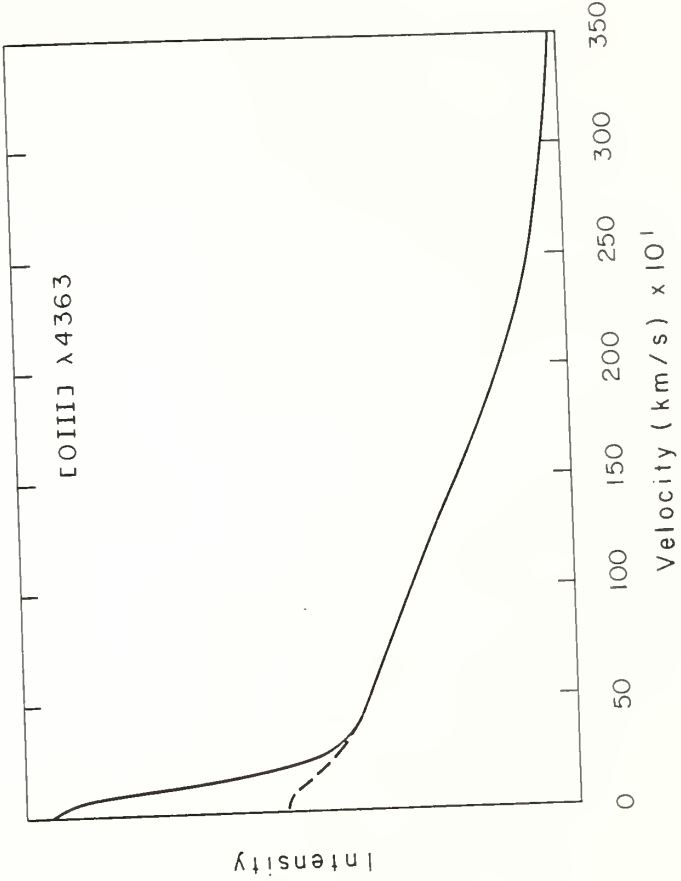


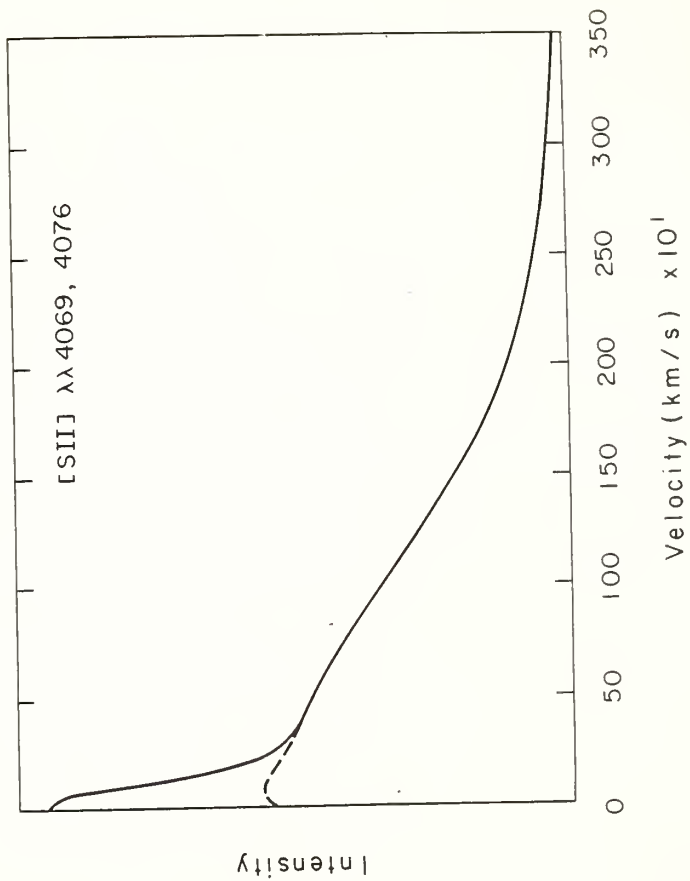














Clouds on the far side of the continuum source will appear brighter, and, if the clouds are infalling, this will yield a stronger blue wing. The same clouds, when they are close to the continuum source, are likely to lose their dust as a result of evaporation and/or the drift of the dust being propelled by radiation pressure through the gas. In any case, the emission of [OIII] $\lambda$ 5007 from the outward leg is much weaker than that during infall as demonstrated in §III. The result is a net blueward asymmetry whose strength depends upon the amount of admixed dust.

### Conclusions

It has been argued that a multi-component NLR is necessary to explain the observed spectra of quasars and Seyfert galaxies. A simple variation in cloud density can provide the low [OIII] $\lambda$ 5007/H $\beta$  and [OIII] $\lambda$ 5007/ $\lambda$ 4363 ratios observed without much affecting the [SII] $\lambda$ 6716/ $\lambda$ 6731 ratio and other low ionization line intensities.

A natural consequence of a gravitational infall model for the BLR is that forbidden line emission is indeed produced over a range of densities, and predicted line intensities are in good agreement with observations.

Several predictions are made which can provide a test of the model. These are:

- 1) Forbidden lines will have extended wings at velocities  $\sim 10^3 \text{ km s}^{-1}$  which may be discernible with high sensitivity

observations.

- 2) The FWZI of forbidden lines should vary, increasing in the order  $[OII]\lambda 3727 < [SII]\lambda\lambda 6716, 6731 < [NII]\lambda 6583 < [OIII]\lambda 5007 < [OI]\lambda 6300 < [NeIII]\lambda 3869 \sim [NeV]\lambda 3426 < [OIII]\lambda 4363 < [SII]\lambda\lambda 4069, 4076$ .
- 3) Intensity ratios formed from the narrow cores of forbidden lines will yield values appropriate for a low density gas, while ratios formed further out in the wings will give values pertaining to higher gas densities. In particular, the ratios  $[OIII]\lambda 5007/H\beta$  and  $[OIII]\lambda 5007/\lambda 4363$  should decrease from  $\sim 26$  and  $\sim 59$  to  $\leq 10$  and  $\leq 15$  respectively with increasing velocity interval from line center.

## C H A P T E R   I V

### THE EXTENDED MODEL

#### Introduction

A gravitational model for the kinematics of the broad emission line gas in quasars and Seyfert nuclei has been shown to satisfactorily reproduce the general features of observed spectra from these objects (Kwan and Carroll 1982; Bradley, Puetter and Hubbard 1983). Other models such as radiative acceleration (Blumenthal and Mathews 1975) or ballistic outflow (Capriotti, Foltz and Byard 1980) are equally successful in reproducing the nominally logarithmic shape of the line profiles. Recent high resolution studies of the profiles in a number of objects, however, have uncovered systematic line width and shape differences, as well as previously noted similarities, among various emission lines (Shuder 1982; Wilkes and Carswell 1982; Wilkes 1983). These features must also be explained by any successful kinematic model.

As the excitation of different lines has different dependences on the physical state of the emitting gas (such as nucleon density and incident radiation intensity), a variety of line shapes implies a variation in the physical conditions throughout the emission line region. Assuming that the physical conditions are correlated with distance from the quasar center (certainly the incident continuum flux, for example), inflow and outflow models will predict markedly different line emission as a function of velocity. The gravitational model dif-

fers from the outflow model in that the former predicts a monotonically decreasing velocity for each emission line cloud with increasing radial distance from the quasar center; the outflow model predicts a velocity changing in the opposite sense. Given a variation of the incident radiation intensity, and perhaps other physical parameters, with radius, a coupling of the emissivity dependences of various sensitive emission lines with the appropriate velocity structures will yield distinctive theoretical profiles which can be used as a test for the nature of the correct kinematics of the emission line gas.

Some advantages of a gravitational model have already been noted. First, it is easier to explain the observed symmetry of Ly $\alpha$  as emitted from an ensemble of optically thick clouds (Kwan and Carroll 1982). A gravitational model can also reasonably account for several anomalous forbidden line intensity ratios as well as for the broad components of [OIII] $\lambda$ 5007 and other forbidden lines (Carroll and Kwan 1983).

In this paper, we wish to further test the model by calculating profiles of the broad permitted and semi-forbidden emission lines. New evidence from recently published data has shown that several systematic line width differences exist between broad lines in the spectrum of a single object. The most prominent of these differences is the greater width of HeI $\lambda$ 5876 compared to H $\beta$  (Shuder 1982). Photoionization calculations show that the intensity ratio HeI $\lambda$ 5876/H $\beta$  increases with increasing incident continuum flux which, for a given object, is  $\propto r^{-2}$  (Netzer 1978; Kwan and Krolik 1981; Kwan 1983). This then implies a greater velocity dispersion at closer distances. Other line width

differences have been noted such as the apparent weakness of the wings of OI $\lambda$ 1304 compared to CIV $\lambda$ 1549 (Wilkes 1983) and the occasionally narrow (relative to the other broad lines) MgII $\lambda$ 2798 line (Ulrich and Boisson 1983; Junkkarinen, Burbidge and Smith 1983). The theoretical emissivity dependences of these lines on the incident continuum flux (Kwan 1983) are again consistent with a greater cloud velocity closer to the continuum source. Observations of the time variation of the CIV $\lambda$ 1549 profile in NGC 4151 provide additional support for this radial velocity dependence in that the wings of the profile were observed to respond earliest and more strongly to continuum variations (Ulrich 1983).

A radial velocity law which increases closer to the continuum source is clearly consistent with a gravitational model. Still, to provide a more stringent test of the correct kinematics, this paper will present a more detailed and physically realistic gravitational model than has heretofore been employed. We shall couple new calculations of the dependence of various line fluxes on physical conditions (Kwan 1983) to the gravitational model in order to demonstrate how the model can account for these new observations as well as to determine new characteristic features.

The more detailed gravitational model takes account of a finite number of infalling clouds as well as the effect of tidal and drag forces on the cloud dynamics. The method for incorporating these effects into the calculations will be described in §II as will considerations of cloud destruction processes. In §III, various model line profiles

will be presented. The impact of a finite cloud number on profile smoothness will also be discussed. Section IV will summarize our results.

### The Model

Our basic premise is that clouds fall in toward the continuum source with a small angular momentum. One characteristic of it is the finite number of clouds that produce the broad-line emission. Previous calculations of line profiles have always assumed that the emission line clouds emit with a delta function profile and that sufficient clouds are present so as to completely fill the available phase space, hence yielding a smooth profile. This paper models clouds of finite extent and computes their velocity profile during the orbit as the clouds are subjected to tidal and drag forces, the latter due to a tenuous quasar wind which confines the clouds. It is obvious that the original large infalling cloud will break up into many smaller cloudlets close to the continuum source. The velocities of the cloudlets, however, are correlated, and, when convolved with line emissivity calculations, produce an emission line profile. The total emission line profile is then obtained by summing the individual profiles from a number of clouds which have been randomly distributed in their orbits so as to ensure a constant mass injection rate.

A complete hydrodynamic solution for the cloud shape as it responds to the changing tidal and pressure forces, including the effects of thermal and ionization balance, would be extremely complex.

The three-dimensional nature of this problem makes even an isothermal computation a formidable task owing to the necessity of following a cloud along its entire orbit, a time period many times greater than the sound crossing time of a typical cloud. Instead, we make the following simplifications. We expect that an initially large cloud (say  $\sim 1$  pc) infalling from  $\sim 1$  kpc will break up into many cloudlets as it approaches the continuum source due to differential radial velocities and/or differential angular momentum across the cloud. Each cloudlet maintains pressure balance with the wind. This breakup cannot proceed very far along the radial direction since each piece must maintain sufficient radial column density to overcome the wind drag force. The radial direction is also the most likely one for compression of the cloud material as it falls inward and its density increases. For these reasons, we assume that a cloud will break up laterally owing to the difference in impact parameters across its face. In this case, each piece retains the full parent cloud column density. We compute orbits for points located on a cross-section of the initial cloud, subject to the wind drag force. A two-dimensional  $(\theta, \phi)$  envelope for the cloud mass is thereby defined as a function of time, and we refer to this as the parent cloud tidal envelope. By dividing the initial cloud into a number of segments and determining their angular position over time, an equation describing the distribution of mass within the envelope can be obtained.

In any model for the emission line region, the majority of emission will arise from those clouds closest to the continuum source.

In outflow models, an arbitrarily large number of arbitrarily sized clouds can be assumed. Gravitational models, however, are limited in that the clouds must be greater than some minimum size in order for gravity to overcome the outward drag force and, hence, for the clouds to fall in at all. Compounding the problem for a gravitational model is that, due to an increasing velocity with closer distance, fewer clouds will be found close to the continuum source. The fraction of parent clouds (close to the continuum source, a parent cloud represents all the cloudlets it breaks up into) within 10 pc is approximately given by the ratio of the free fall time from 10 pc to that from the starting radius of 1 kpc:  $\sim \tau_{ff}(10 \text{ pc}) / \tau_{ff}(1 \text{ kpc}) \sim 10^{-3}$  of the total cloud number will lie within 10 pc of the quasar center. In our models (see §III), there are typically tens of parent clouds within 10 pc. Since a velocity space extending from  $\sim -10,000$  to  $+10,000 \text{ km s}^{-1}$  must be covered, each of those parent clouds must have a velocity dispersion  $\Delta v \gtrsim 1000 \text{ km s}^{-1}$  in order to more or less fill the available velocity space.

Dispersion in projected velocity space results either from velocity differences among the cloudlets or from wrapping of the tidal envelope about the quasar so that a range of projection angles is present. It turns out that if the initial cloud size at 1 kpc is  $\sim 1.5 \text{ pc}$ , our standard cloud size, the angular momentum gradient across the cloud is not very great if due only to the difference in impact parameters. Consequently, as the parent cloud breaks up, the resulting velocity dispersion among the cloudlets is too small to produce an acceptably



smooth profile. By allowing for a small ( $\sim 10 \text{ km s}^{-1}$ ) gradient in the infall velocity across the cloud face, however, the angular momentum difference is greatly accentuated, and the clouds will be stretched sufficiently to yield a relatively smooth profile.

The equations of motion for a cloudlet with angular momentum per unit mass  $\vec{l}$ , total energy per unit mass  $E \equiv 1/2 |\vec{v}|^2 - GM_Q/r$ , and nucleonic column density  $N_c$  are:

$$\begin{aligned} \frac{d\vec{l}}{d\theta} &= \frac{r^2}{|\vec{l}|} (\vec{a}_{\text{drag}} \times \vec{r}) \\ \frac{dE}{d\theta} &= \frac{r^2}{|\vec{l}|} (\vec{a}_{\text{drag}} \cdot \vec{v}) \\ \frac{dr}{d\theta} &= \frac{r^2}{|\vec{l}|} v_r \\ \frac{d\theta}{dt} &= \frac{|\vec{l}|}{r^2} \end{aligned}$$

with the cloudlet velocity  $\vec{v} = v_r \hat{r} + v_\theta \hat{\theta}$  and,

$$\vec{a}_{\text{drag}} = - \frac{\rho_w}{\mu_N m_H N_c} \left[ \vec{v} - v_w \hat{r} \right]^2 \frac{(\vec{v} - v_w \hat{r})}{|\vec{v} - v_w \hat{r}|}.$$

The above equations have been written in circular coordinates  $(r, \theta)$  in the orbital plane, and  $\rho_w$  is the wind mass density,  $M_Q$  the quasar mass,  $\mu_N$  the mean nucleonic atomic weight,  $m_H$  the mass of hydrogen, and  $\vec{v}_w = |\vec{v}_w| \hat{r}$  the wind velocity. The relative wind-cloudlet velocity is supersonic with respect to the wind for the standard model parameters so that the drag force is due to the wind ram pressure only.

Several models for a quasar wind have been discussed in the literature (Beltrametti and Perry 1980; Weymann et al. 1982). The detailed behaviour of a wind solution depends upon the assumed acceleration mechanism and on the treatment of thermal balance. Rather than choose a specific published model, we assume an isothermal wind expanding at its sound speed. This is a fair approximation in any case, and it will serve well to illustrate the qualitative results which we wish to emphasize in this paper. We fix the value of  $\rho_w$  at a radius of 1 pc by requiring pressure balance between the cloud front and the incident wind, i.e.  $\rho_w = \rho_c T_c / 2T_w$ , where  $\rho_c$  is chosen to agree at 1 pc with numerical calculations of the cloud density (Kwan and Krolik 1981).

The major dynamical result of the wind drag is to trap clouds with less than a certain angular momentum, causing them to spiral into the quasar center. The escape or trapping of a cloud is more sensitive to the angular momentum than to the cloud energy since it is the angular momentum which primarily determines the distance of closest approach. A cloud falling closer to the quasar experiences a greater drag due to the greater wind density and gravitational velocity. Most of the energy and angular momentum loss consequently occurs near the peri-quasar point which lies at a distance of  $r_{pq} = \ell^2 / 2GM_Q = 1 \text{ pc} (v_0 b_0 / 10000 \text{ km s}^{-1} \times \text{pc})^2 / (M_Q / 10^{10} M_\odot)$ , where the orbital ellipticity has been set at  $\epsilon = 1$ , and  $b_0$  is the cloud impact parameter and  $v_0$  is the cloud velocity at infinity. For the standard model we present in §III, pertinent parameters are  $N_c = 1 \times 10^{23} \text{ cm}^{-2}$ ,  $M_Q = 10^{10} M_\odot$ ,  $T_w = 10^{10} \text{ K}$ ,  $\rho_w = 2 \times 10^3 \mu_N m_H (1 \text{ pc}/r)^2$ , and  $v_0 = 300 \text{ km s}^{-1}$ . By computing orbits

with various impact parameters, it was found that clouds with average  $b_0 < 50$  pc were trapped. In deriving this, it has been assumed that once clouds pass through their peri-quasar point they will expand in response to the decreasing external pressure. The cloud column density then decreases as  $(r_{pq}/r)^{4/3}$ , and the drag acceleration increases. The critical column density below which the drag force becomes greater than the gravitational force is  $N_c \approx p_w r^2 / (\mu_N m_H G M_Q) \approx 3.8 \times 10^{22} \text{ cm}^{-2}$  with  $p_w = \rho_w v_w^2$  being the wind pressure. Clouds decreasing their column density below this value due to expansion will be swept away by the wind. This result has been verified by numerical experiment.

If all clouds are trapped and fall into the quasar, the mass accretion rate can be estimated as follows. The standard model cloud has mass  $m_c \sim (1.5 \text{ pc})^2 \times 10^{23} \text{ cm}^{-2} \times \mu_N \times m_H = 2360 M_\odot$  with  $\mu_N = 1.3$  for a 10% He abundance by number. This yields a total ensemble mass for  $2 \times 10^4$  clouds (the standard model number) of  $M = 4.7 \times 10^7 M_\odot$ . The free fall time from 1 kpc distance is  $\tau_{ff} \sim 2 \times 10^6$  years. The mass accretion rate, if all clouds are trapped, is then  $\dot{M} \sim 23.5 M_\odot \text{ yr}^{-1}$ . The mass outflow in the wind, for comparison, is  $\dot{M}_w \sim 2 \times 10^3 \text{ cm}^{-3} \times \mu_N \times m_H \times 4\pi (1 \text{ pc})^2 \times 1.3 \times 10^9 \text{ cm s}^{-1} \sim 11.8 M_\odot \text{ yr}^{-1}$ . A large fraction of the mass in the clouds could be lost and blown out with the wind, and the actual mass accretion rate onto the quasar would then be correspondingly reduced. It turns out that only models including some mass loss from the clouds seem capable of reproducing the observed line profiles (see §III). We discuss two possible mass loss mechanisms below.

During the breakup of the parent clouds, material is likely to be

lost as sub-critical column density pieces are blown away by the wind. This process is analogous to the ablation of material from clouds, especially if the breakup is triggered by some form of Rayleigh-Taylor process. Ablation has been discussed in some detail by Christiansen, Pacholczyk and Scott (1977) and Christiansen and Scott (1983). The former authors derive an approximate ablation time  $t_{ab} \sim (\lambda^2 \rho_c / v^2 \rho_w)^{1/2}$  where  $\lambda$  is the wavelength of the perturbation, and  $v$  is the relative wind-cloud velocity. This time is a measure of the speed with which rippling perturbations on the cloud surface are swept around the sides of the cloud and subsequently stripped off. It presupposes the ready availability of such perturbations, however, as due to Rayleigh-Taylor or Kelvin-Helmholtz instability for instance. Christiansen, Pacholczyk and Scott (1977) have indicated that this ablation time is in general shorter than the growth time of a Rayleigh-Taylor instability. For the standard model parameters,  $t_{ab} < 10^5$  years, and this time is only weakly dependent upon the cloud's radial position. This time is longer than the free fall time for  $r < 160$  pc so that ablation is not likely to be important at closer distances.

A second mass loss mechanism is evaporation of cloud material. This has been discussed extensively by Cowie and McKee (1977) and by Balbus and McKee (1982). A number of different solutions exist for the mass loss rate, dependent upon conditions in the hot intercloud gas. The latter authors defined a parameter  $\sigma_0' = 1.3 \times 10^4 T_{\Gamma_e}^2 / (n_w r_c)$  which is roughly the ratio of the mean free path of a hot electron in the hot gas to the cloud dimension  $r_c$ . The definition of  $T_{\Gamma_e}$  is  $T_{\Gamma_e} \equiv \min(T_w,$

$2.6 \times 10^9$  K), and  $n_w$  is the intercloud electron density. When  $\sigma_0' > 100$ , the hot electrons penetrate into the cloud itself, and the evaporative outflow must be modeled as a two-fluid system with a suprathermal component. This situation is the appropriate one for the quasar emission line region, but several solutions are possible in this regime (Balbus and McKee 1982).

The applicable suprathermal evaporative solution is a function of both  $\sigma_0'$  and  $T_w$ . For our standard conditions,  $T_w = 10^{10}$  K and  $\sigma_0' \sim 10^8$  at 1 kpc distance. The parameter  $\sigma_0'$  will remain approximately constant since  $n_w \propto r^{-2}$  and the radial thickness  $r_c \propto r^2$  if compression of the cloud is primarily one-dimensional. Checking these values with figures 7 and 8 from Balbus and McKee (1982) yields two possible solutions dependent upon the specific value of  $\sigma_0'$ . For  $\log \sigma_0' < 5$ , Balbus and McKee's STC solution is valid, STC signifying suprathermal, thermal conduction dominated. This solution describes a situation where the hot electrons are at too high a temperature for them to deposit much energy in the cloud by Coulomb collisional heating. Radiative losses in the cloud will instead be balanced by thermal conduction through the cloud boundary (the authors did not consider photoionization processes). The evaporation time, including the effects of the suprathermal ion heating of the cloud, is  $t_{\text{evap}} = 1.8 \times 10^7 (r_c/1 \text{ pc})^{5/4} (n_w/10^3 \text{ cm}^{-3})^{1/4} \times (10^4/T_c)$  years with  $T_c$  the cloud temperature. Even if  $t_{\text{evap}}$  varies as  $r^2$ , the free fall time will be shorter over most of the orbit.

The estimated value for  $\sigma_0'$  in our standard model is  $\sim 10^8$ . A supersonic evaporative flow solution does not exist when  $\log \sigma_0' > 5$ ,

however, and the intercloud pressure is greater than that of the cloud halo in this case. This is due to the inability of the mildly relativistic wind electrons at  $T_w > 3 \times 10^9$  K to effectively couple with the cloud gas via Coulomb collision. The hot electrons cannot transfer heat, but neither can they provide a confining momentum transfer (i.e. pressure). Some process which excludes the ions from the cloud, however, such as a plasma streaming instability or a magnetic field should provide a pressure great enough to suppress the outflow. In this case, clouds will likely be stable against thermal evaporation. A gas kinetic analysis of this regime is probably necessary to conclusively decide this issue (Balbus and McKee 1982).

We do not know how to realistically incorporate the above physical effects quantitatively into our model. Thus, to approximately account for mass loss due to the processes of evaporation and ablation, we simply assume that the mass of a cloud varies with distance from the quasar center as  $m \propto (r/r_0)^s$ , where  $r_0$  is the initial cloud distance, and  $s$  is a parameter to be chosen. Note that for a constant column density, the cloud mass is proportional to the cloud area.

The line emission from a cloud is a function of the absorbed ionizing continuum. For optically thick clouds, the fraction of the total continuum luminosity absorbed is equal to the cloud covering factor as observed from the ionizing continuum source. Kwan (1983) has computed the emergent intensities of various lines as a function of the incident ionizing flux. His results were integrated over the face of each parent cloud envelope, weighted by the amount of mass present.

Rather than attempt to identify individual cloudlets, the available cloud mass was assumed to be distributed along the parent cloud envelope according to a functional form derived as follows. The initial cloud face was divided into a number of segments of equal mass. The position of each boundary point was determined as a function of time, and the angular mass density between each pair of points was computed. A smooth curve could then be fitted to describe the fraction of the total cloud mass within a given angular interval along the envelope. The covering factor contributed by the hypothetical cloudlets in an angular interval along the cloud envelope was then determined from the cloud mass within that interval (equivalent to the cloud area), but reduced by the mass loss factor as described above and by the geometrical dilution of  $r^{-2}$  from the continuum source. The computed intensities were distributed in velocity space according to the projected velocity in the line of sight direction at each point of the interval. The contributions from all intervals were then summed to produce a resultant profile for the parent cloud. For reference, the standard cloud with initial size 1.5 pc ultimately stretches over a distance of some 20 pc yielding a velocity dispersion of  $\Delta v \sim 20,000 \text{ km s}^{-1}$  for an orbit which is observed edge on.

The total emission line profiles were obtained by summing the resultant profiles from all members of an ensemble of individual parent clouds. These spectra are discussed in the next section, as are derivations of the different selected parameters.

### Model Profiles

Model line profiles for the emission lines Ly $\alpha$ , H $\delta$ , MgII $\lambda$ 2798, HeI $\lambda$ 5876, CIV $\lambda$ 1549, and CIII]  $\lambda$ 1909 were computed as described in §II. Spherical symmetry in the distribution of orbits was assumed. A central mass of  $M_Q = 10^{10} M_\odot$ , a wind temperature  $T_w = 10^{10}$  K, a wind nucleon density  $n_w = 2 \times 10^3 (1 \text{ pc}/r)^2 \text{ cm}^{-3}$  (assuming a cloud frontal temperature  $T_c = 2 \times 10^4$  K), a constant cloud nucleon column density  $N_c = 10^{23} \text{ cm}^{-2}$ , and a cloud nucleon density of  $n_c = 2 \times 10^9 (1 \text{ pc}/r)^2 \text{ cm}^{-3}$  were taken as standard parameters. Clouds were injected at a distance of 1 kpc with average energy and angular momentum per unit mass  $E = 1/2(300 \text{ km s}^{-1})^2$  and  $\ell = 300 \text{ km s}^{-1} \times b_0 \text{ pc}$  respectively, with  $b_0$  a parameter. A  $10 \text{ km s}^{-1}$  linear gradient in the infall velocity was established across the face of the cloud such that the smallest impact parameter point had the largest velocity ( $305 \text{ km s}^{-1}$ ).

The selected cloud density and column density were chosen so as to agree with those parameters derived for the broad-line clouds from theoretical computation (Kwan and Krolik 1981; Kwan 1983). At a distance of  $\sim 1 \text{ pc}$  where most of the broad-line emission occurs, the adopted central mass will give a velocity of  $\sim 10^4 \text{ km s}^{-1}$ , a typical line width. The high wind temperature was selected for no better reason than to keep the wind mass outflow rate smaller than the cloud mass infall rate (see §II).

A mass loss exponent  $s = 0.5$  was also chosen as standard. Exponents ranging from  $\sim 0.3$  to  $0.7$  produce similar profiles. A value



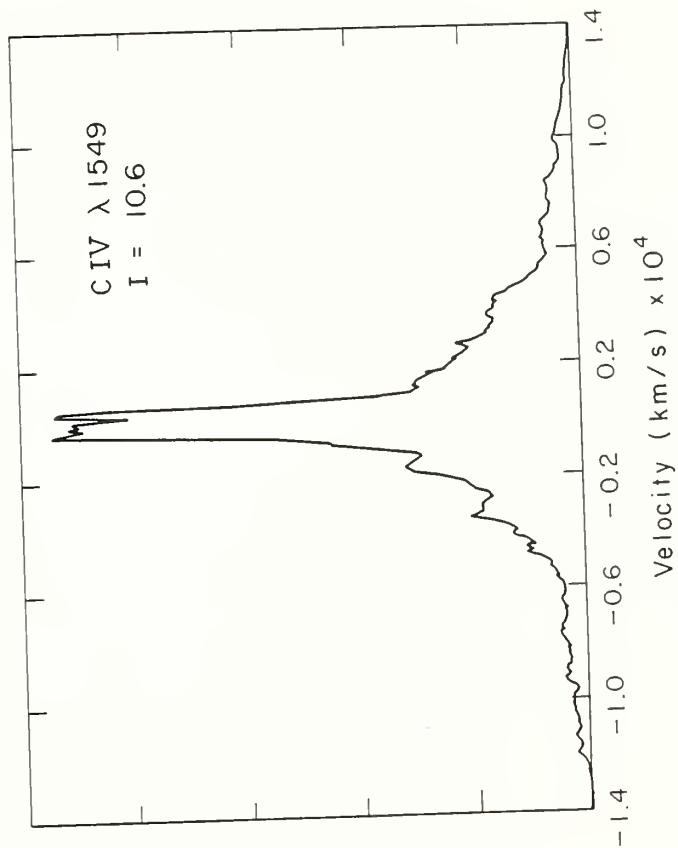
$s = 0.0$ , corresponding to conservation of mass, is definitely unacceptable since then the line wings produced are much too strong. Also, the profile is very jagged. This is because we impose a constraint that the total cloud ensemble covering factor be  $\leq 0.1$ ; with  $s = 0.0$ , the total number of infalling clouds is too small. For  $s = 0.5$ , a total of  $2 \times 10^4$  clouds with an initial diameter of 1.5 pc was judged to be optimal.

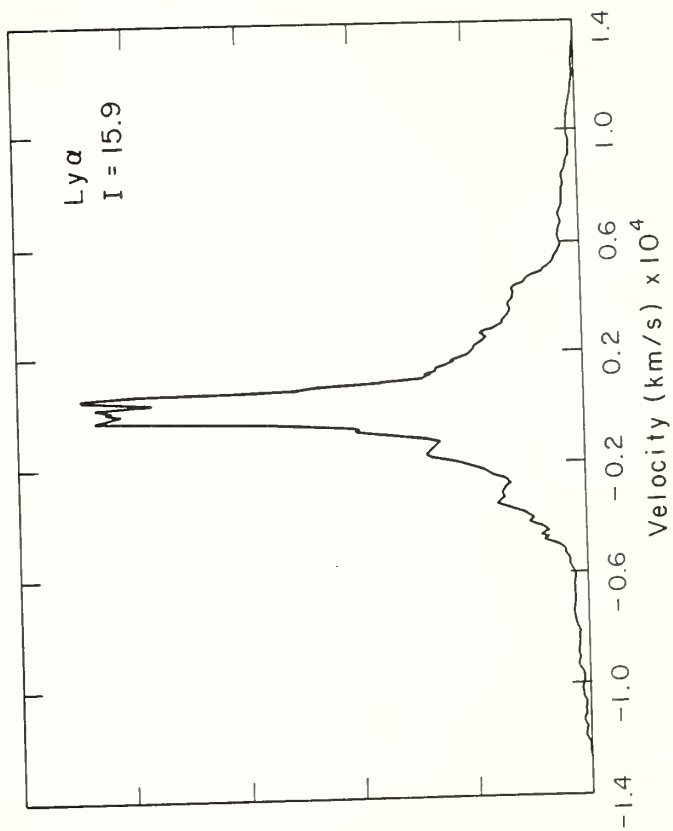
Figure 10 shows a series of line profiles for the standard parameters and average  $b_0 = 40$  pc. The clouds spiral inward in this case, never returning beyond 2 pc. Several complete orbits are necessary for the angular momentum to reduce to zero, but integration is halted when the velocity equals  $14,000 \text{ km s}^{-1}$ . Any mass which attains a velocity greater than this is considered to be instantaneously destroyed. This occurs here at  $\theta \sim 4\pi$  and  $r \sim 0.06$  pc, where  $\theta = 0$  is the initial direction of cloud infall. At the time when half the parent cloud has passed beyond this point, the trailing edge still lies back at a distance of some 20 pc.

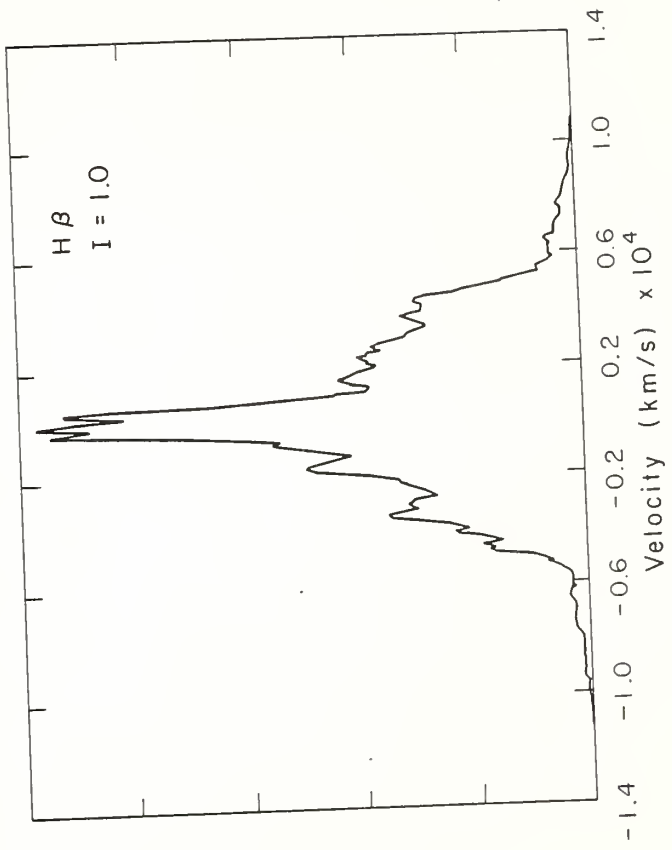
The profiles in figure 10 have been computed with the same random cloud distribution so that the correlation of features from one line to the next may be noted. "Noise" on the shoulders of Ly $\alpha$  is reproduced with varying strength in other lines of the series. This fluctuation is contributed by parent clouds closer to the quasar than  $\sim 10$  pc (as measured by the position of the mean mass point), and these are relatively few in number ( $\sim 85$ ; this number is greater than that estimated in §II owing to the extra time allowed by the orbital motion).

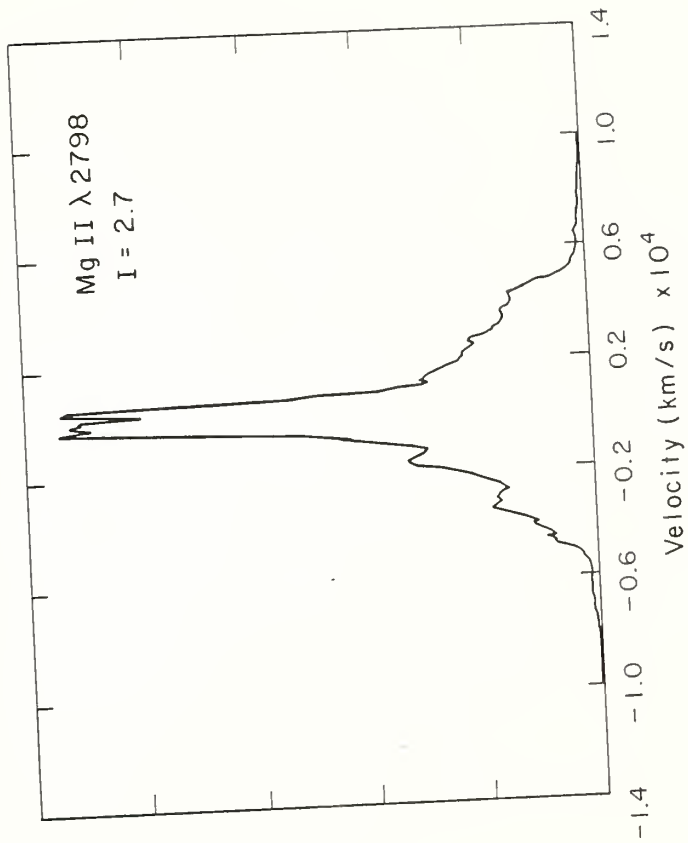
Consequently, any line which is predominantly produced close to the

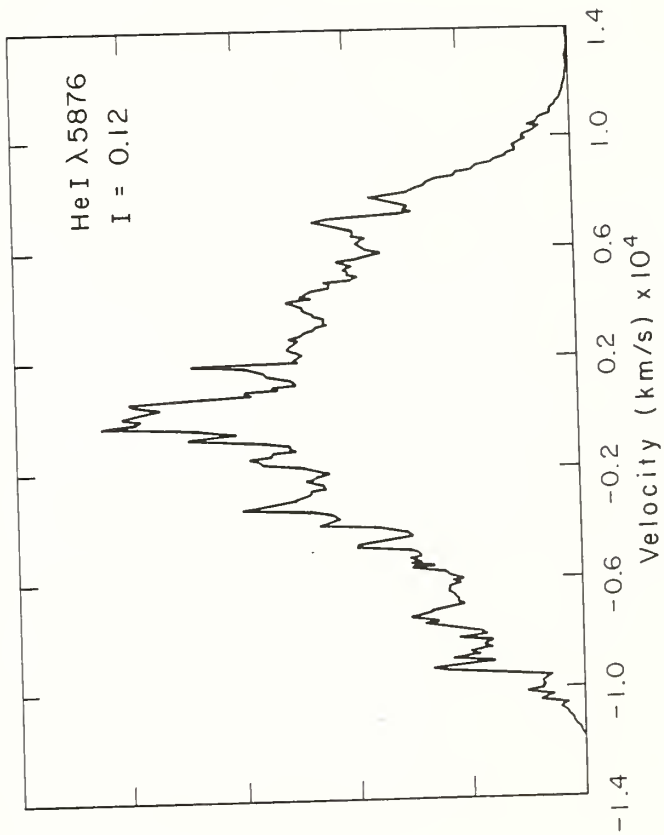
Fig. 10. Model profiles for the standard case with  $2 \times 10^4$  clouds of size  $r_c = 1.5$  pc and with average angular momentum  $\ell = 300 \text{ km s}^{-1} \times 40$  pc. Clouds are trapped and fall into the quasar in this case.  $I$  is the integrated line intensity relative to that of  $H\beta$ , and positive velocities designate a redshift with respect to line center. All axes are plotted with a linear scale.

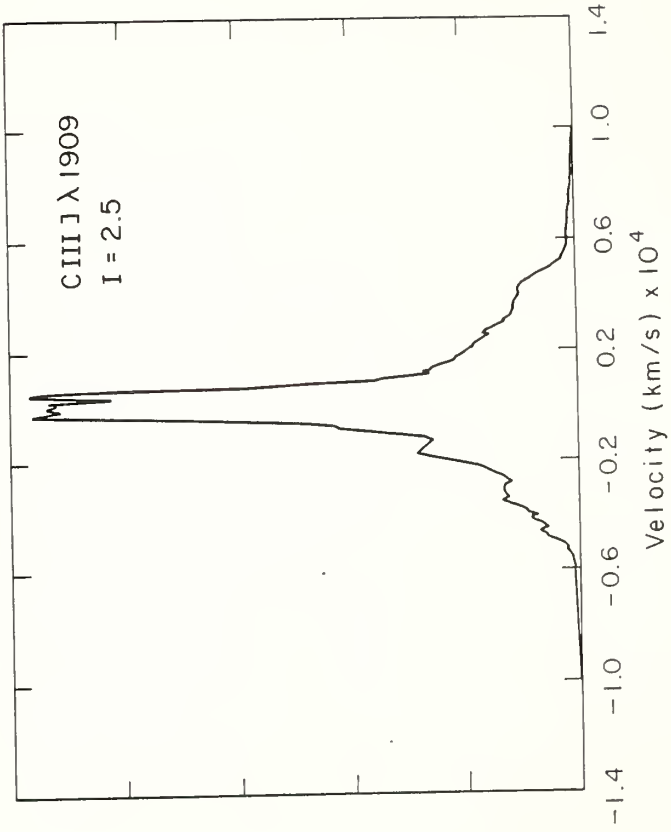












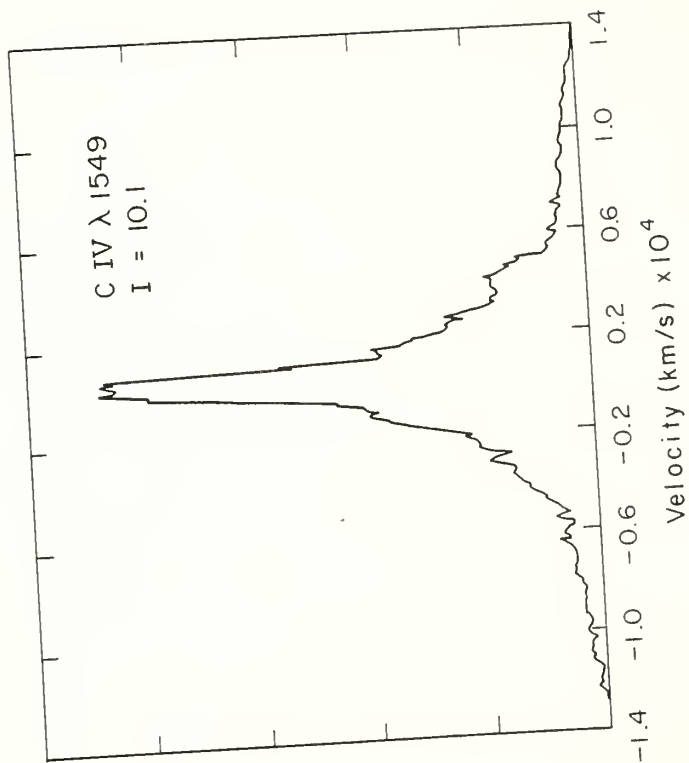


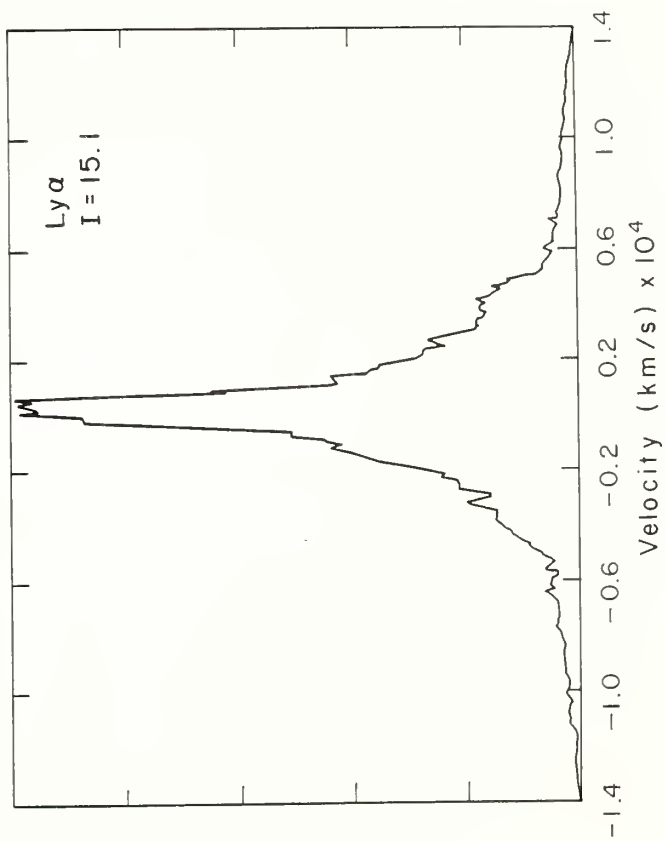
quasar will be noisier than the others. HeI $\lambda$ 5876 is an example. The low plateau of extended emission seen in the Ly $\alpha$  and CIV $\lambda$ 1549 profiles beyond  $\sim 6,000 \text{ km s}^{-1}$  is contributed by those portions of the clouds which are wrapped around the quasar at distances  $< 1 \text{ pc}$ . This emission enhances the profile wings above those of a logarithmic profile.

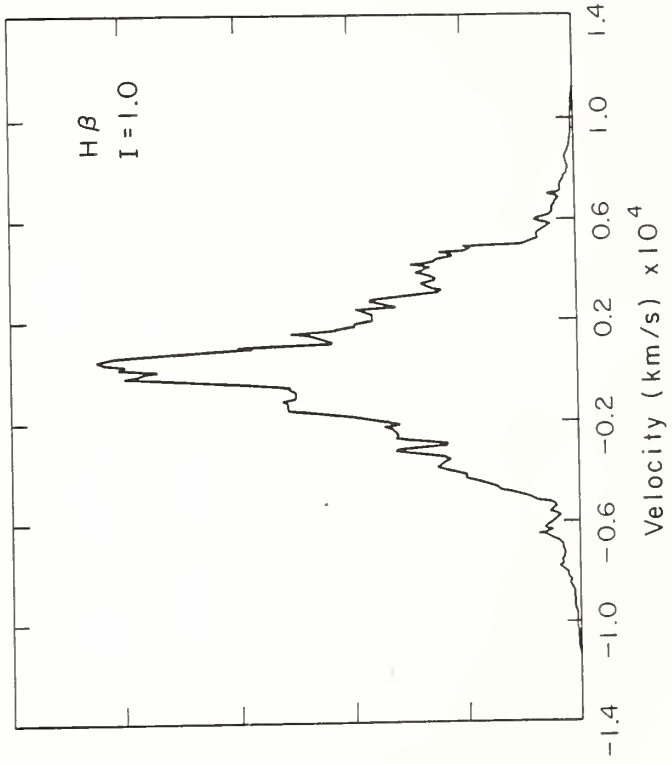
Steplike structure is seen on the shoulders of most profiles. This is a consequence both of the small cloud number at higher velocities and of the peculiar individual cloud profile shape. The profile contributed by that portion of a parent cloud which is wrapped around the quasar is similar to that of a narrow rotating ring. The profile produced by a thin, isotropically emitting, rotating ring has been given by Shields (1978) as  $f_v \propto (1 - (v/v_{\text{max}})^2)^{-1/2}$  where  $v = v_{\text{max}} \cos \theta$  is the projected velocity with  $v_{\text{max}} = v_{\text{rot}} \sin i$ ,  $\theta$  is the angle between the velocity vector and the line of sight direction,  $i$  the inclination, and  $v_{\text{rot}}$  the rotation velocity. This function has a minimum at zero velocity and peaks sharply at the extreme velocities. Beyond  $v_{\text{max}}$  the profile drops identically to zero. The sum of a number of such profiles will be "spiky" relative to a like number of summed flat topped profiles (a flat topped profile results from a radially moving shell). The high velocity edges of these spikes will be sharper than the low velocity side, giving the appearance of a steplike structure.

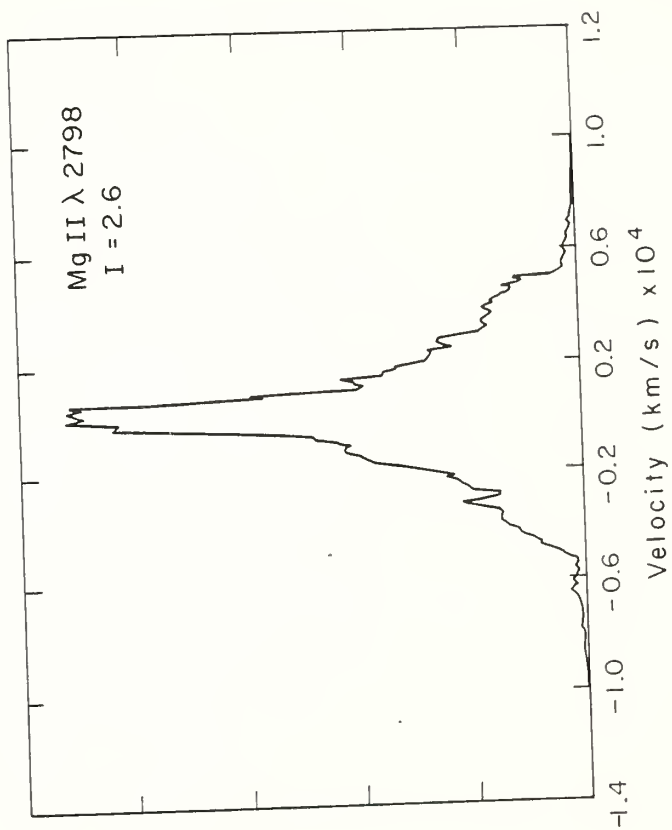
Figure 11 depicts a second random distribution of clouds with the same parameters as figure 10. Notice how the noise peaks have shifted due to a different positioning of the closer clouds and that these features are once again reproduced from profile to profile. In figures

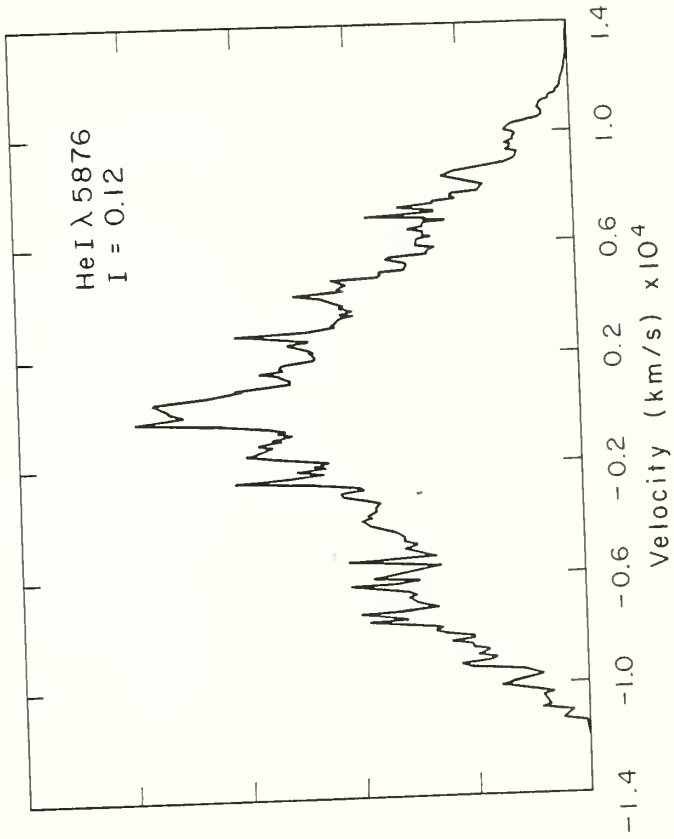
Fig. 11. Model profiles with the same parameters as Fig. 1 but with a different random cloud distribution.

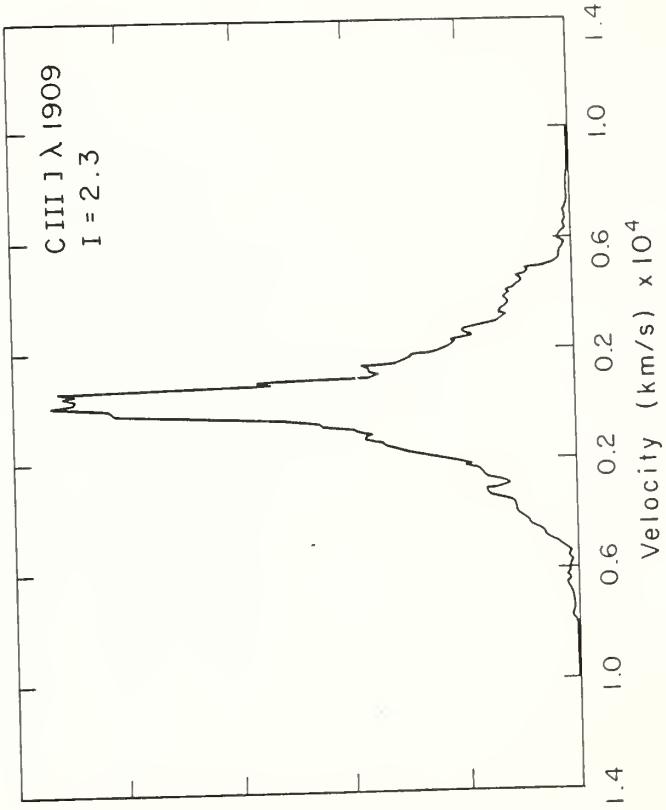












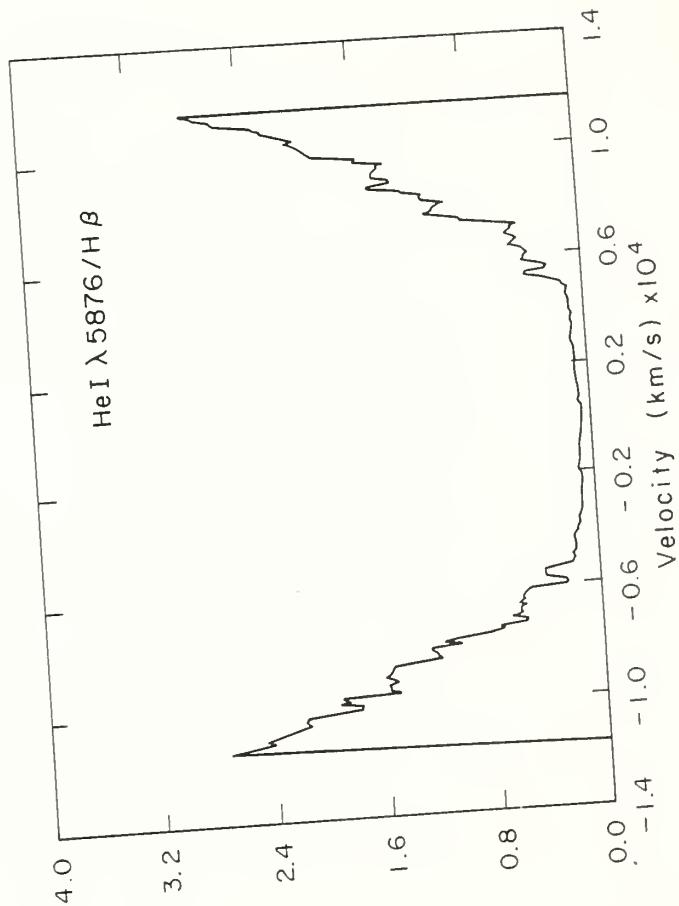


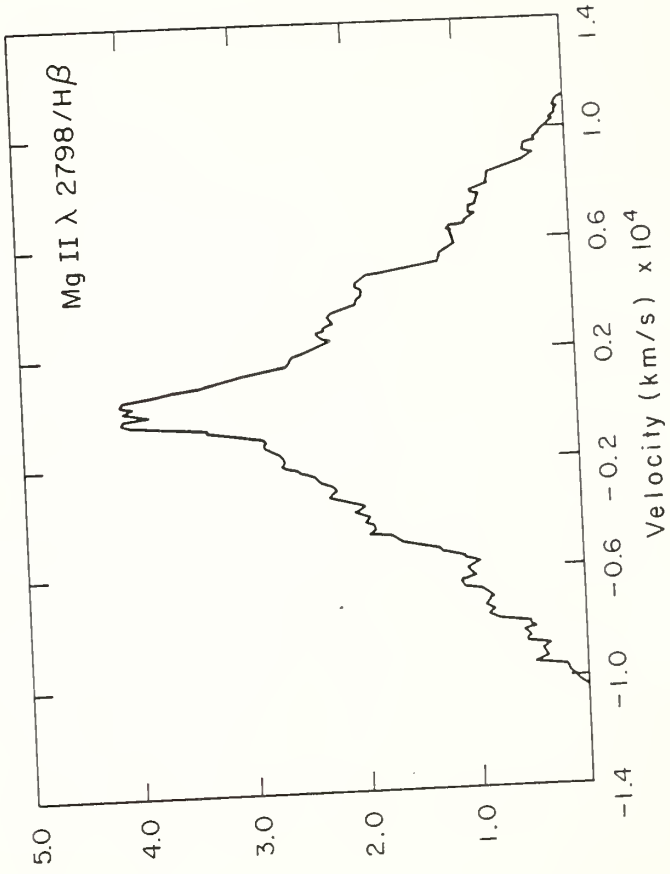
10 and 11, the integrated line flux relative to that of H $\beta$  is printed on the diagram, and no important difference in the ratios is evident between the two cloud distributions.

In both sets of profiles, it is obvious that HeI $\lambda$ 5876 is much broader than H $\beta$  and that MgII $\lambda$ 2798 is somewhat narrower. A comparison of the profile of CIII] $\lambda$ 1909 which is suppressed at densities  $> 2 \times 10^9 \text{ cm}^{-3}$  with the CIV $\lambda$ 1549 profile reveals an obvious difference only in the far wings. Following Shuder (1982), we demonstrate the line width differences more clearly by dividing one profile by another to depict the line ratio as a function of velocity. This has been done for the line ratios HeI $\lambda$ 5876/H $\beta$ , MgII $\lambda$ 2798/H $\beta$ , and CIII] $\lambda$ 1909/CIV $\lambda$ 1549, and these are plotted in figure 12. As discussed by Kwan (1983), the HeI $\lambda$ 5876/H $\beta$  ratio increases with increasing incident continuum flux, equivalently with increasing velocity in a gravitational model, due largely to the increased excitation from trapping of HeI $\lambda$ 10830. The MgII $\lambda$ 2798/H $\beta$  ratio decreases since MgII $\lambda$ 2798 thermalizes more easily than H $\beta$  so that its relative share of the cooling diminishes with increasing continuum flux. The final ratio exhibited, CIII] $\lambda$ 1909/CIV $\lambda$ 1549, decreases at high velocity due to collisional suppression of CIII] $\lambda$ 1909. This effect has been observed in NGC 4151 (Penston et al. 1981).

The profiles produced by a cloud ensemble with average  $b_0 = 70 \text{ pc}$  are much more similar to each other and to those generated by Kwan and Carroll (1982). They are displayed in figure 13. In this case, the clouds escape following parabolic orbits. The maximum velocity is only

Fig. 12. Several diagnostic line ratios are plotted as a function of velocity from line center.





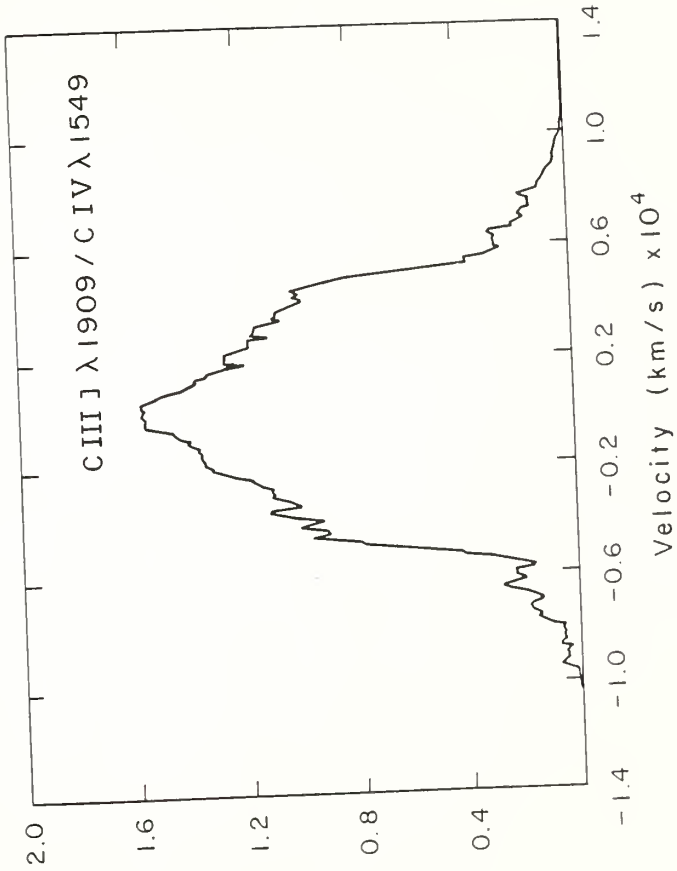
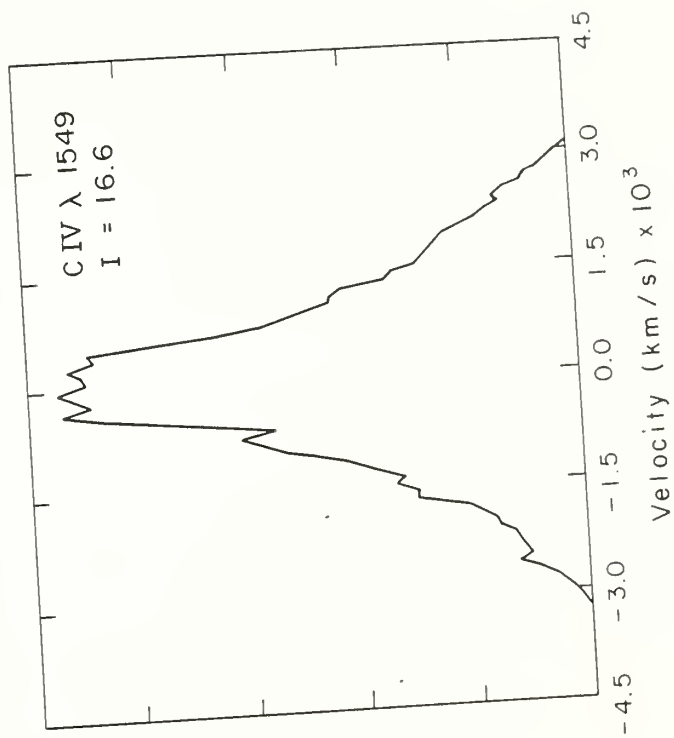
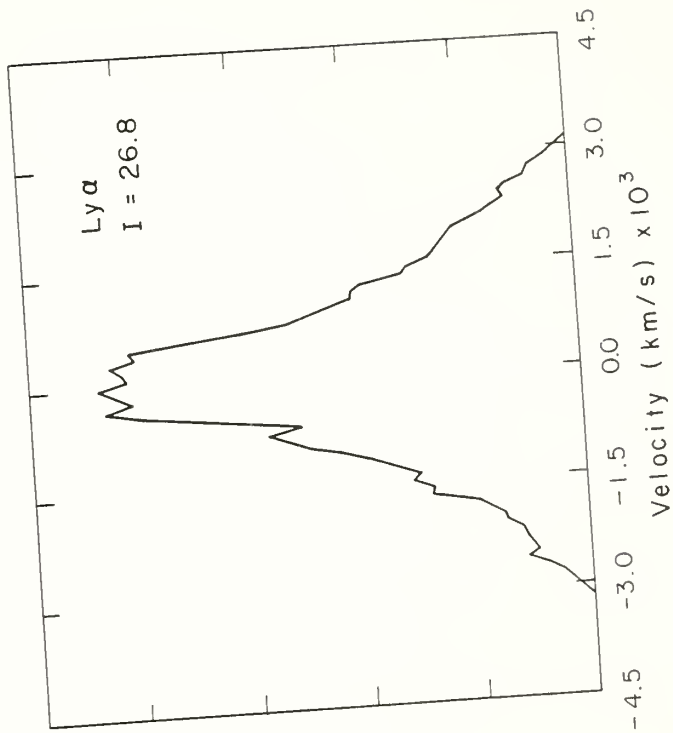
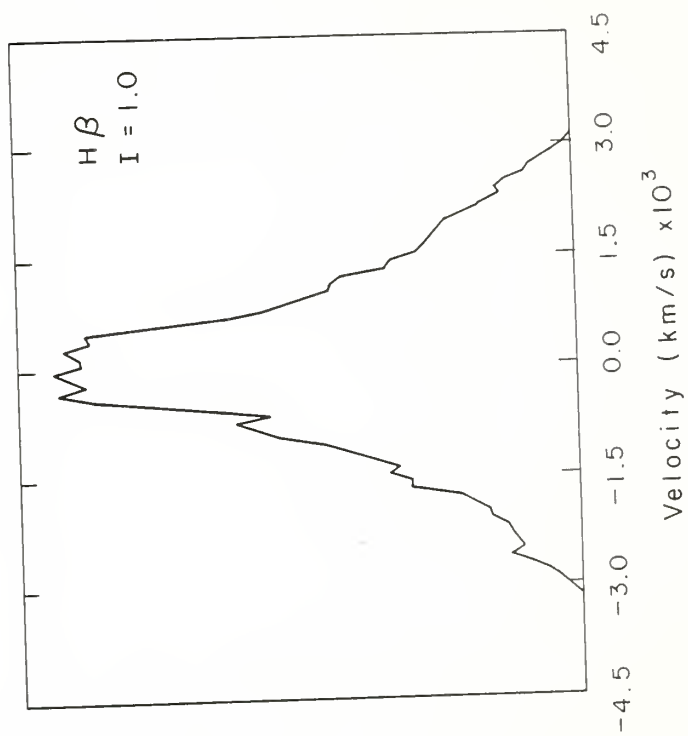


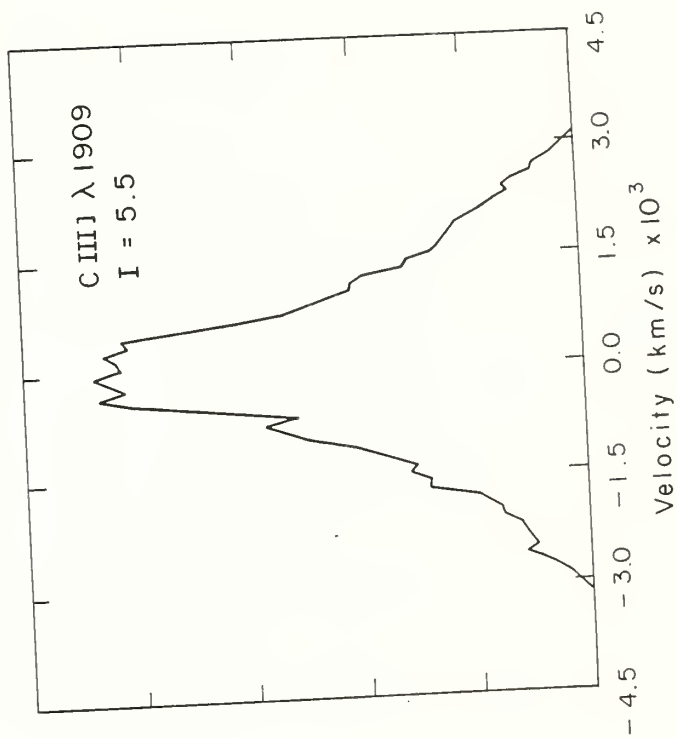
Fig. 13. Model profiles for the standard case but with average angular momentum  $\ell = 300 \text{ km s}^{-1} \times 70 \text{ pc}$ . Clouds escape following parabolic orbits.











$\sim 4,000 \text{ km s}^{-1}$ , however, since the peri-quasar point lies at  $\sim 5 \text{ pc}$  for this angular momentum. An averaging of figure 10 or 11 with figure 13 would enhance the core of the trapped cloud profiles, thereby producing a better approximation to a logarithmic shape.

All of the profiles presented above assumed isotropic emission from each cloudlet. This may not be the case, particularly for Ly $\alpha$ . Figure 14 depicts a Ly $\alpha$  profile generated for three different angular emissivity dependences and  $b_0 = 40 \text{ pc}$ . The first assumes Ly $\alpha$  to be emitted isotropically (case a), the second assumes an angular emissivity law,

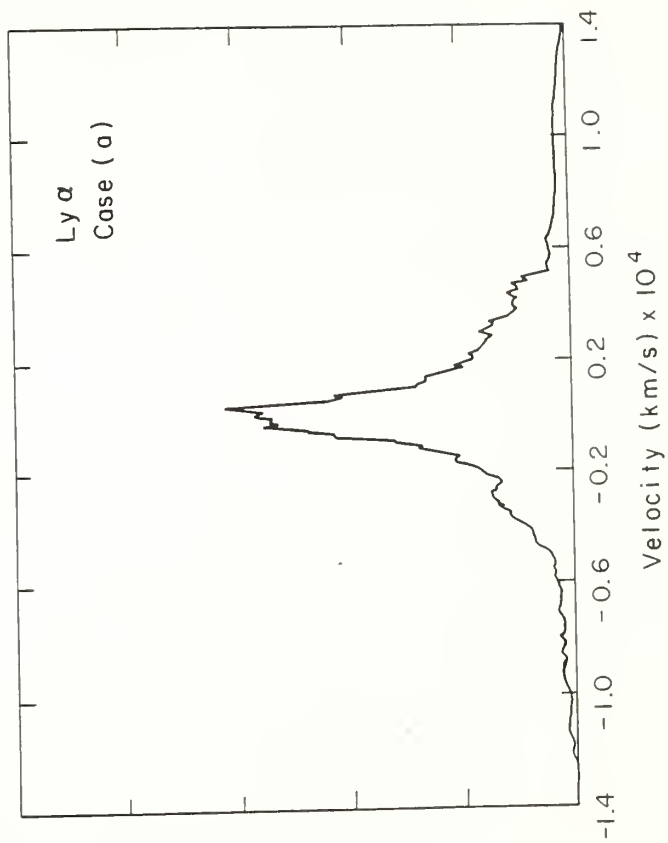
$$\phi(\theta) = \begin{cases} 1 & 0 < \theta < \pi/2 \\ 0 & \pi/2 < \theta < \pi \end{cases} \quad (\text{case b})$$

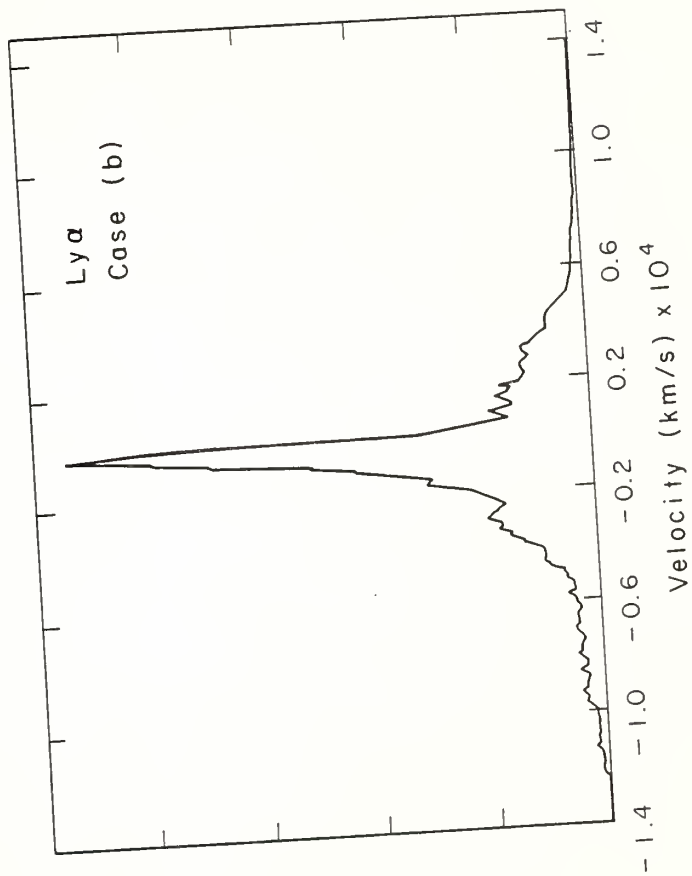
and the third has an angular dependence,

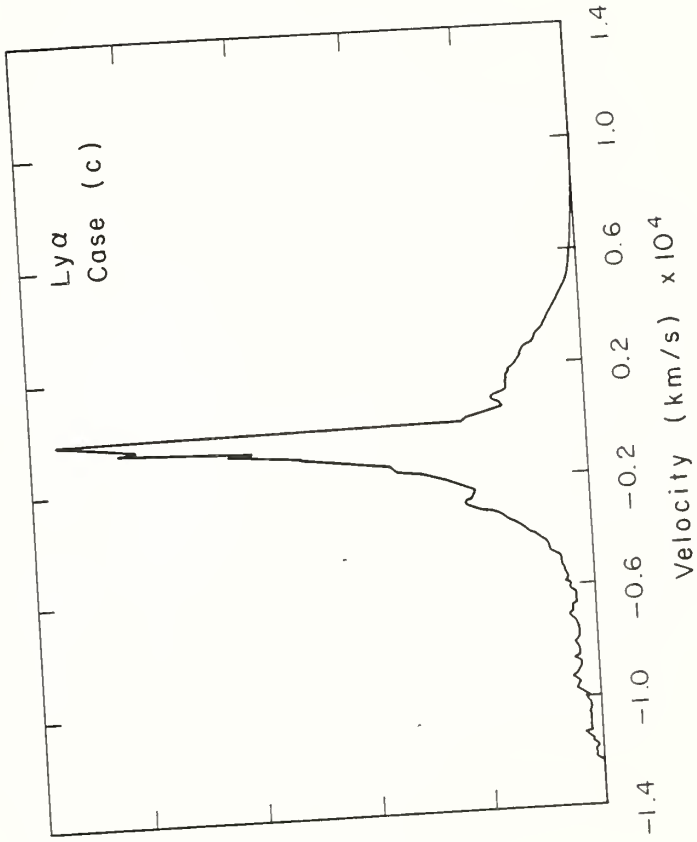
$$\phi(\theta) = \begin{cases} 2\cos\theta & 0 < \theta < \pi/2 \\ 0 & \pi/2 < \theta < \pi \end{cases} \quad (\text{case c})$$

where  $\theta$  is the angle between the line of sight and the cloud radial position vector. The lack of an outward leg for a trapped cloud means that the Ly $\alpha$  emission in cases (b) or (c) will not be exactly symmetric. Case (b) eliminates emission from the red radial leg of the infalling clouds; this primarily affects the core of the profile. The far red wing is lost as well because the highest velocity portion of the orbit is also predominantly radial due to angular momentum loss. Case (c) additionally assumes that the emission is proportional to the projected cloud area in the line of sight direction. This effect further

Fig. 14. Ly $\alpha$  profiles are plotted for different angular emissivity dependences as described in the text. Case (a) is for isotropic emission, case (b) is for optically thick clouds, and case (c) includes the effects of the projected cloud area.





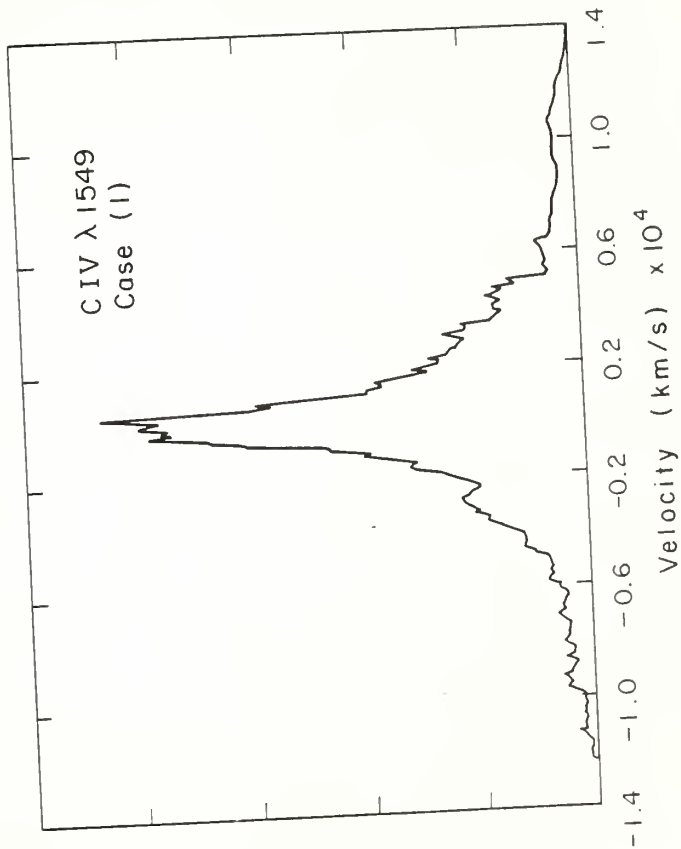


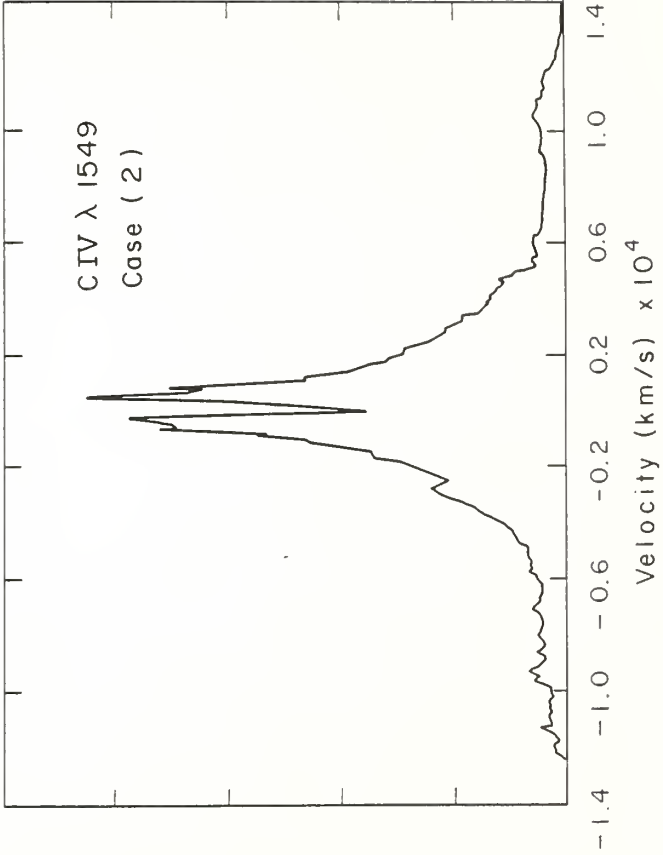
weakens the core by suppressing the contribution from high inclination orbits, but it also reduces the profile wings since they are contributed primarily by the orbiting clouds which are close to the quasar and which are moving in the line of sight direction i.e. with  $\theta = \pi/2$ . Both case (b) and case (c) produce similar profiles. Case (c) is smoother since the projection effect weakens the horns of the profile from a rotating ring (see above); for a thin rotating ring and the angular emissivity dependence given by case (c), the resultant profile is flat topped. The asymmetry in both cases is not too bad, particularly if an escaping cloud ensemble is averaged with it. The addition of an  $\text{OVI}\lambda 1218$  component with strength  $\sim 7\%$  that of  $\text{Ly}\alpha$  (Kwan and Krolik 1981) and with a shape similar to that of  $\text{CIV}\lambda 1549$  does not significantly alter the profiles.

Other lines which are very optically thick may emit with an anisotropic angular dependence of the form  $\phi(\theta) = \{ 2|\cos\theta| \}$  for  $0 < \theta < \pi$ .  $\text{CIV}\lambda 1549$  is a likely candidate, and it is presented for this case and for the case of isotropic emission as well in figure 15. The result of this projection effect is to weaken the peak of the profile. The trough around zero velocity will likely be filled in by the narrow-line region contribution to  $\text{CIV}\lambda 1549$ . Even so, the  $\text{CIV}\lambda 1549$  profile will have a weaker peak than  $\text{Ly}\alpha$ . Note that the  $\text{Ly}\alpha$  asymmetry would predict a blueshift of the centroid of  $\text{Ly}\alpha$  emission relative to that of  $\text{CIV}\lambda 1549$ . The projection effect also smooths the  $\text{CIV}\lambda 1549$  profile as discussed above. A possible problem is that this projection effect also broadens  $\text{CIV}\lambda 1549$  relative to  $\text{CIII}\lambda 1909$  which itself is not likely to be



Fig. 15. CIV $\lambda$ 1549 profiles plotted for the case of isotropic emission ( case(1) ) and for the case where the emission is proportional to the projected illuminated cloud area ( case(2) ).





affected. The profile of CIII] $\lambda$ 1909 is found to be narrower in some objects (Ulrich and Boisson 1983) and line contamination may obscure the difference in other observed spectra (Gaskell, Shields and Wampler 1981; Wilkes 1983).

#### Summary

The parabolic orbital model for the quasar emission line region (Kwan and Carroll 1982) has been extended and improved. Rather than concentrate on reproducing in detail the observed profiles which must depend upon the unknown cloud angular momentum distribution, we have attempted to demonstrate the qualitative effects of a finite cloud size and number, of the dynamical drag of the confining intercloud wind, and of the dependence of line excitation on physical conditions upon the generated line profiles.

The main dynamical effect of the wind drag is to trap clouds of low angular momentum ( $l < 300 \text{ km s}^{-1} \times 50 \text{ pc}$ ) so that they fall into the quasar. This leads to an asymmetry in the Ly $\alpha$  profile such that the core and far wings on the blue side are stronger.

The trapping of some portion of the infalling clouds also provides the possibility for a blue asymmetry in the other broad lines. A blue shift has been observed between the high ionization broad lines on the one hand and the low ionization broad lines and forbidden narrow lines on the other (Gaskell 1982). The ability of this model to account for these differences will be discussed in a later paper.

The positive correlation between cloud velocity and incident

radiation intensity in a gravitational model provides a natural explanation for the relatively broader HeI $\lambda$ 5876 and relatively narrower MgII $\lambda$ 2798 lines as compared with H $\beta$ .

The small number of clouds contributing to high velocities in a gravitational model produces variable structure in the shoulders and wings of various emission lines. This structure is correlated from one line to the next. As this structure depends upon the positioning of the highest velocity clouds, a time variation in this structure is expected as the clouds shift in their orbits. The nature of these variations and the response of the different lines to continuum fluctuations will also be investigated in a later paper.

A relatively smooth line profile is obtained despite the small number of clouds which contribute the majority of the emission in a gravitational model. This is accomplished owing to the breakup of each parent cloud due to the differential angular momentum of its constituent parts. The velocity dispersion between the fragment cloudlets allows the velocity space to be more or less uniformly filled. Some mass loss from the clouds seems necessary in order to produce acceptable profiles. This allows a greater number of clouds to be included without violating the total covering factor constraint of  $f \sim 0.1$ .

A gravitational origin for the kinematics of the broad-line emission region in quasars and Seyfert galaxies has been shown to be capable of accommodating the observed similarities and differences among the various emission lines. Hopefully, this study will motivate further observations with high spectral resolution and signal-to-noise which

can further test the model.

C H A P T E R   V  
S U M M A R Y   A N D   F U T U R E   W O R K

This dissertation advocates a gravitational origin for the kinematics of the broad-line emission regions of quasars and active galactic nuclei. Given that the infalling material has some non-zero angular momentum, this model naturally and reasonably provides a symmetric Ly $\alpha$  profile, even from an ensemble of optically thick clouds. In chapter II, theoretical profiles were generated and compared with logarithmic line shapes, and the pros and cons of this model and others proposed were discussed.

In chapter III, we next examined the forbidden line spectrum of quasars and Seyfert galaxies in light of the various proposed kinematic models for the broad-line regions of these objects. Gravitational infall models predict significant forbidden line emission at velocities  $< 10^3$  km s $^{-1}$ . Different emission line widths are obtained for different lines dependent upon their respective critical densities for collisional de-excitation; lines with higher critical densities will have broader profiles. Ballistic outflow and radiative acceleration models, on the other hand, are found to produce negligible forbidden line emission at these velocities.

If the gravitationally infalling clouds are confined by a hot wind, as seems likely, then the forbidden line emission produced by those clouds will be characteristic of high density ( $> 10^6$ ) gases. The large contribution of this high density gas to the total forbidden

line emission in gravitational infall models allows the low [OIII] $\lambda$ 5007/H $\beta$ <sub>n<sub>rw</sub></sub> ( $\sim 10$ ) and [OIII] $\lambda$ 5007/ $\lambda$ 4363 ( $\sim 15$ ) ratios observed in quasars and Seyfert galaxies to be neatly explained as due to the combined emission from the infalling high density clouds ( $\lambda$ 5007/H $\beta$ <sub>n<sub>rw</sub></sub>  $\sim 7.3$ ,  $\lambda$ 5007/ $\lambda$ 4363  $\sim 5$ ) and the low density narrow-line region ( $\lambda$ 5007/H $\beta$ <sub>n<sub>rw</sub></sub>  $\sim 26$ ,  $\lambda$ 5007/ $\lambda$ 4363  $\sim 59$ ). The observed density sensitive [SII] $\lambda$ 6716/ $\lambda$ 6731 ratio, which gains little emission from the infalling clouds, retains its observed low density value of  $\sim 1$ , characteristic of low density ( $\sim 10^4 \text{ cm}^{-3}$ ) gas.

Forbidden line profiles and total intensities for the parabolic-orbital model were presented and compared with existing observations.

In chapter IV, the parabolic-orbital model (Kwan and Carroll 1982) for the broad emission line regions of quasars and Seyfert galaxies is extended and improved to include the effects of a finite infalling cloud number and size. Disruption of the cloud by the differential angular momentum across its face results in a large velocity dispersion among the resulting fragment cloudlets. This velocity dispersion compensates for the small number of clouds at high velocity so that a fairly smooth profile is obtained.

The drag of a confining intercloud wind is also considered. The major dynamical effect of this drag is to trap clouds with less than a certain angular momentum,  $\ell < 300 \text{ km s}^{-1} \times 50 \text{ pc}$  for our standard model parameters. The trapping of clouds produces an asymmetry in the Ly $\alpha$  profile due to the absence of an outward leg for the trapped clouds. The asymmetry is reduced by the spiralling of the trapped cloud



material, and it shows up mainly in the core and far wings of the profile. Further reduction in the asymmetry can be obtained if an escaping cloud ensemble is averaged in as well.

The dependence of various line emissivities on the incident ionizing flux has been computed by Kwan (1983). His results are convolved with the cloud velocity dispersions, and the resulting emission line profiles demonstrate that the gravitational model can reproduce the observed broadness of  $\text{HeI}\lambda 5876$  relative to  $\text{H}\beta$  (Shuder 1982). Profiles for  $\text{Ly}\alpha$ ,  $\text{Mg}\lambda 2798$ ,  $\text{CIV}\lambda 1549$ , and  $\text{CIII}\lambda 1909$  were also generated and compared to existing observations.

At this moment in the progress of quasar research, theoretical predictions have outstripped the available observations to test them. It is hoped that this work will motivate further high resolution and high signal to noise observations which will be able to distinguish between the between the different models.

Additional theoretical work which can be done with the parabolic-orbital model includes an investigation of the origin of observed line asymmetries, in particular of the apparent blueshift of the high ionization lines relative to the low ionization and forbidden lines. A detailed prediction of the time variation in the line profile structure in this model would also be useful. In a more speculative vein, an investigation into the question of whether the luminosity and lifetime differences between quasars and Seyfert galaxies (quasars all died at approximately the epoch of galaxy formation) can be explained in terms of a different angular momentum distribution for the infalling gas.

Seyferts are invariably spiral galaxies which have a high average angular momentum, hence implying a relatively slow, but steady, mass infall rate. The host galaxy type for quasars is still indeterminate, but a rapid central collapse would be consistent with the low angular momentum of elliptical galaxies. Perhaps a theoretical model incorporating an evolving infalling mass rate and angular momentum distribution function, coupled with greater observational efforts to determine the galaxy morphology associated with quasars, if any, could provide answers to some of these questions.

While much work remains to be done, a gravitational origin for the kinematics of the emission line regions of quasars and active galactic nuclei is continually gaining observational support. The parabolic-orbital model, in particular, is the most successful of the competing kinematic models in explaining recent observational evidence.

BIBLIOGRAPHY

- Aldrovandi, S.M.V., and Pequignot, D. 1973, Astr. Ap., 25, 137.
- Balbus, S.A., and McKee, C.F. 1982, Ap. J., 252, 529. Baldwin, J.A. 1975, Ap. J., 201, 26.
- Baldwin, J.A. 1977, M.N.R.A.S., 178, 67P.
- Baldwin, J.A., and Netzer, H. 1978, Ap. J., 226, 1.
- Baliunas, S.L., and Butler, S.E. 1980, Ap.J.(Letters), 235, L45.
- Baluja, K.L., Burke, P.G., and Kingston, A.E. 1980, J. Phys. B., 13, 829.
- Baluja, K.L., and Hibbert, A. 1980, J. Phys. B., 13, L327.
- Beltrametti, M., and Perry, J.J. 1980, Astr. Ap., 82, 99.
- Bhatia, A.K., Doschek, G.A., and Feldman, U. 1979, Astr. Ap., 76, 359.
- Blumenthal, G.R., and Mathews, W.G. 1975, Ap. J., 198, 517.
- Boggess, A. et al. 1979, Ap. J.(Letters), 230, L131.
- Bradley, S.E., Puetter, R.C., and Hubbard, E.N. 1983, preprint.
- Butler, S.E., and Dalgarno, A. 1979, Ap. J., 234, 765.
- \_\_\_\_\_ . 1980, Ap. J., 241, 838.
- Butler, S.E., Heil, T.G., and Dalgarno, A. 1980, Ap. J., 241, 442.
- Canfield, R.C., and Puetter, R.C. 1980, Ap. J.(Letters), 236, L7.
- Capriotti, E., Foltz, C., and Byard, P. 1980, Ap. J., 241, 903.
- \_\_\_\_\_ . 1981, Ap. J., 245, 396.
- Carroll, T.J., and Kwan, J. 1983, Ap. J., 274, 000.
- Christiansen, W.A., Pacholczyk, A.G., and Scott, J.S. 1977, Nature, 266, 593.
- Cowie, L.L., and McKee, C.F. 1977, Ap. J., 211, 135.

- Davidson, A.F., Hartig, G.F., and Fastie, W.G. 1977, Nature, 269, 203.
- Davidson, K. 1975, Ap. J., 195, 285.
- Davidson, K., and Netzer, H. 1979, Rev. Mod. Phys., 51, 715.
- Doschek, G.A., Feldman, U., Bhatia, A.K., and Mason, H.E. 1978, Ap. J., 226, 1129.
- Dufton, P.L., Berrington, K., Burke, P., and Kingston, A. 1978, Astr. Ap., 62, 111.
- Eissner, W., and Seaton, M.J. 1974, J. Phys. B., 7, 2533.
- Ferland, G.J., and Netzer, H. 1979, Ap. J., 229, 274.
- Ferland, G.J., Netzer, H., and Shields, G.A. 1979, Ap. J., 232, 382.
- Ferland, G.J. 1981, Ap. J., 249, 17.
- Field, G.B., and Steigman, G. 1971, Ap. J., 166, 59.
- Field, G.B., Arp, H., Bahcall, J.N. 1973, The Redshift Controversy, (Reading, Mass.: W.A. Benjamin.)
- Flower, D.R., and Nussbaumer, H. 1975a, Astr. Ap., 42, 144.
- \_\_\_\_\_ . 1975b, Astr. Ap., 45, 145.
- Gaskell, C.M., Shields, G.A., and Wampler, E.J. 1981, Ap. J., 249, 443.
- Gaskell, C.M. 1982, Ap. J., 263, 79.
- Giles, K. 1979, M.N.R.A.S., 187, 49P.
- Gould, R.J. 1978, Ap. J., 219, 250.
- Grandi, S.A., and Phillips, M.M. 1979, Ap. J., 232, 659.
- Grandi, S.A. 1980, Ap. J., 238, 10.
- Green, R.F., Pier, J.R., Schmidt, M., Estabrook, F.B., Lane, A.L. and Wahlquist, H.D. 1980, Ap. J., 239, 483.

- Heckman, T.M., Miley, G.K., van Breugel, W.J.M., and Butcher, H.R.  
 1981, Ap. J., 247, 403.
- Henry, R.J.W. 1970, Ap. J., 161, 1153.
- Jackson, A.R.G. 1973, M.N.R.A.S., 165, 53.
- Junkkarinen, V.T., Burbridge, E.M., and Smith, H.E. 1983, Ap. J., 265,  
 51.
- Koski, A.T. 1978, Ap. J., 223, 56.
- Krolik, J.H., and McKee, C.F. 1978, Ap. J. Suppl., 37, 459.
- Krolik, J.H., McKee, C.F., and Tarter, C.B. 1981, Ap. J., 249, 422.
- Kwan, J., and Krolik, J.H. 1979, Ap. J.(Letters), 233, L91.  
 \_\_\_\_\_ . 1981, Ap. J., 250, 478.
- Kwan, J., and Carroll, T.J. 1982, Ap. J., 261, 25.
- Kwan, J. 1983, preprint.
- Mathews, W.G. 1982, Ap. J., 252, 39.
- Matthews, T.A., and Sandage, A.R. 1963, Ap. J., 138, 30.
- Miley, G.K., and Heckman, T.M. 1982, Astr.Ap., 106, 163.
- Netzer, H. 1982, M.N.R.A.S., 198, 589.
- Nussbaumer, H. 1970, Ap. J., 166, 411.  
 \_\_\_\_\_ . 1971, Ap. J., 170, 93.  
 \_\_\_\_\_ . 1972, Astr. Ap., 16, 77
- Nussbaumer, H., and Storey, P.J. 1978, Astr. Ap., 64, 139.  
 \_\_\_\_\_ . 1979, Astr. Ap., 74, 244.  
 \_\_\_\_\_ . 1981, Astr. Ap., 99, 177.
- Oke, J.B., and Zimmerman, B. 1979, Ap. J., 231, L13.
- Osmer, P.S., and Smith, M.G. 1980, Ap. J. Suppl., 42, 333.

- Osterbrock, D.E. 1974, Astrophysics of Gaseous Nebulae, (San Francisco: Freeman.)
- \_\_\_\_\_. 1977, Ap. J., 215, 733.
- \_\_\_\_\_. 1978, Proc. Nat. Acad. Sci., 75, 540.
- Osterbrock, D.E., and Wallace, R.K. 1977, Ap. Letters, 19, 11.
- Pelat, D., and Alloin, D. 1980, Astr. Ap., 81, 172.
- \_\_\_\_\_. 1982, Astr. Ap., 105, 335.
- Pelat, D., Alloin, D., and Fosbury, R.A.E. (1981), M.N.R.A.S., 195, 787.
- Penston, M.V. et al. 1981, M.N.R.A.S., 196, 857.
- Pequignot, D., and Aldrovandi, S.M.V. 1976, 50, 141.
- Phillips, M.M. 1976, Ap. J., 208, 37.
- Pradhan, A.K. 1974, J. Phys. B., 7, L503.
- \_\_\_\_\_. 1976, M.N.R.A.S., 177, 31.
- \_\_\_\_\_. 1978, M.N.R.A.S., 183, 89P.
- Reilman, R.F., and Manson, S.T. 1979, Ap. J. Suppl., 40, 815.
- Richstone, D.O., Ratnatunga, K., and Schaeffer, J. 1980, Ap.J., 240, 1.
- Schmidt, M. 1963, Nature, 197, 1040.
- Seaton, M.J. 1958, Rev. Mod. Phys., 30, 979.
- \_\_\_\_\_. 1975, M.N.R.A.S., 170, 475.
- Shields, G.A. 1978, Pittsburgh Conf. on BL Lacertae Objects, ed. A.M. Wolfe, (Pittsburgh: University of Pittsburgh.) p. 257.
- Shuder, J.M., and Osterbrock, D.E. 1981, Ap. J., 250, 55.
- Shuder, J.M. 1982, Ap. J., 259, 48.
- Shull, J.M. 1979, Ap. J., 234, 761.

- Soifer, B.T., Neugebauer, G., Oke, J.B., and Matthews, K. 1981, Ap. J., 243, 369.
- Storey, P. 1981, M.N.R.A.S., 195, 27P.
- Trimble, V. 1975, Rev. Mod. Phys., 47, 877.
- Turnshek, D.A., Weymann, R.J., Liebert, J.W., Williams, R.E., and Strittmatter, P.A. 1980, Ap. J., 238, 488.
- Ulrich, M.H., and Boisson, C. 1983, Ap. J., 267, 515.
- Ulrich, M.H. 1983, XI Texas Symposium on Relativistic Astrophysics, in press.
- Ward, M.J. 1978, Ph.D. thesis, University of Sussex.
- Weisheit, J.C., Shields, G.A., and Tarter, C.B. 1981, Ap. J., 245, 405.
- Weymann, R.J. 1981, talk presented at Caltech Conference on the Broad-Line Region of Quasars and Active Galactic Nuclei.
- Weymann, R.J., Scott, J.S., Schiano, A.V.R., and Christiansen, W.A. 1982, Ap. J., 262, 497.
- Wiese, W.L., Smith, M.W., and Glennon, B.M. 1966, Atomic Transition Probabilities, Vol. 1 (NBS NSR DS - NBS4).
- Wilkes, B.J., and Carswell, R.F. 1982, M.N.R.A.S., 201, 645.
- Wilkes, B.J. 1983, preprint.
- Wu, C.C. 1977, Ap. J. (Letters), 217, L117.
- Wu, C.C., Boggess, A., and Gull, T.R. 1981, Ap. J., 247, 449.
- \_\_\_\_\_. 1983, Ap. J., 266, 28.

## APPENDIX

The numerical code employed to compute the emission line intensities incorporated methods and assumptions similar to those of Kwan and Krolik (1981). Since these have been detailed elsewhere, we shall not discuss them here. Instead, atomic data used will be referenced, and some particular physical processes important in low density gases will be pointed out.

Photoionization cross-sections for HI and HeI, good to X-ray energies, were computed from Kwan and Krolik's (1981) fit to theoretical and experimental data using Seaton's (1958) two-term interpolation formula. Other atomic cross-sections were taken from the compilation of Reilman and Manson (1979). Photoionization cross-sections from excited states of many species were taken from Henry (1970). The most important of these was photoionization from the  $2D$  state of NI. This state has an ionization threshold, which at 12.1 eV, is below the Lyman edge. For this reason, significant photoionization of NI can occur in the extended ionized zone; as a result the total emission of  $[NII]\lambda 6583$  is increased considerably.

Secondary ionization of hydrogen and helium by suprathermal photoelectrons was included, with the parameters taken from the work of Shull (1979). This is the dominant mode of ionization for hydrogen in the extended ionized zone, much as thermal collisional ionization is at higher densities (Kwan and Krolik 1981).

All hydrogen charge exchange reactions listed by Butler and Dalgarno (1979, 1980), Butler, Heil and Dalgarno (1980) and



Baliunas and Butler (1980) were used, as well as that for  $O^+$  (Field and Steigman 1971). These reactions are very important in determining the ionization structure, but unfortunately the rates are not always well determined and some important reactions may have been overlooked.

Radiative recombination coefficients were taken from Gould (1978) when possible and from Aldrovandi and Pequignot (1973) otherwise. Dielectronic recombination coefficients were taken from Storey (1981) and Aldrovandi and Pequignot (1973); the tabulated rates were reduced as described by Davidson (1975) in order to account for collisional reionization.

Collisionally excited line cooling was included for many other lines besides those listed in Table 1. Collision strengths were taken from many sources including Baluja et al. (1980a, 1980b), Giles (1979), Dufton et al. (1978), Bhatia et al. (1979), Jackson (1973), Doschek et al. (1978), Pradhan (1974, 1976, 1978), Osterbrock and Wallace (1977), Pequignot and Aldrovandi (1976), Eissner and Seaton (1974), and Seaton (1975). Einstein A-coefficients were taken from Wiese et al. (1966), Nussbaumer (1970, 1971, 1972), Nussbaumer and Storey (1978, 1979, 1981), Baldwin and Netzer (1978), Flower and Nussbaumer (1975a, 1975b) and Dufton et al. (1978). The most recent data for each line was chosen, and final recourse was taken to Osterbrock (1977) for data unavailable elsewhere (for the OI A-coefficients, for instance). Collisional production of Ly  $\alpha$  is a strong coolant in the extended ionized zone, and excitation rates for this process were found in Krolik and McKee (1979).

Solar element abundance (Trimble 1975) was adopted in the ratio by number H: He: C: N: O: Ne: Mg: Si: Fe: S = 1:  $10^{-1}$ :  $3.5 \times 10^{-4}$ :  $10^{-4}$ :  $7 \times 10^{-4}$ :  $10^{-4}$ :  $3 \times 10^{-5}$ :  $3 \times 10^{-5}$ :  $3 \times 10^{-5}$ :  $1.5 \times 10^{-5}$  respectively.

